Generated using LaTeX template two-column layout. This work has been submitted for publication. Copyright in this work may be transferred without further notice, and this version may no longer be accessible. This work was conducted independently and is presented as a preprint. Thank you for your understanding.

arXiv:2604.20222v4 [physics.ao-ph] 5 Aug 2026

Localized Tornado Outbreak at the Upstream of a Tropical Easterly Wave in Camarines Norte, Philippines (13 September 2025)

Generich H. Capuli[a,b]

[a] *Numerical Modelling Section, Research & Development and Training Division, Department of Science and Technology - Philippine Atmospheric, Geophysical, and Astronomical Services Administration, Brgy. Central, Quezon City 1100, Metro Manila, Philippines*
[b] *Project Severe Weather Archive of the Philippines, Quezon City, Philippines*

ABSTRACT: On 13 September 2025 around 22 UTC, a localized tornado outbreak commenced and affected eastern Philippines, producing significant damage across Camarines Norte. The event developed within an atypical easterly severe weather regime, characterized by warm, moist southeasterly flow and strong low-level wind shear associated with an approaching easterly wave trough. The upstream segment of the inverted trough acted as a focus for convective initiation, where a pronounced vorticity convergence zone enhanced low-level rotation. Environmental wind profiles exhibited strongly curved-highly streamwise hodographs, indicating a kinematic environment favorable for supercell development and tornadogenesis. At least five vortices were identified, three of which were confirmed as tornado-producing supercells through combined damage surveys and Doppler radar analysis. The Magang tornadic supercell was rated IF2.5 (EF3-equivalent) with ~2 km damage path, while the Cahabaan and Napilihan tornadic supercells was rated IF1 (EF1-equivalent) with the Cahabaan storm producing a ~3 km path length. The remaining vortices were assigned IF0 (EF0-equivalent). Notably, these tornadoes occurred simultaneously, highlighting the presence of multiple discrete supercells within the same mesoscale environment, with Magang and Cahabaan supercells in close proximity potentially contributing to tornadogenesis through localized inflow–outflow balance interactions. Dual-polarization Doppler radar observations revealed key storm-scale features such as Z_{DR} and K_{DP} columns. Furthermore, the Magang tornado exhibited strong velocity couplet signatures co-located with a pronounced correlation coefficient (ρ_{HV}) depression, consistent with a debris signature. Meanwhile, the Cahabaan tornado-producing supercell displayed a well-defined bounded weak echo region (BWER), indicative of a strong, sustained updraft. This study integrates reanalysis data, satellite imagery, lightning observations, and dual-polarization radar to document the first known tornado outbreak and simultaneous tornadic supercells in the Philippines within an easterly severe weather environment.

Keywords: Atmospheric Environment, Supercells, Tornadoes, Remote Sensing - Satellite and Radar Analysis, Damage Assessment

1. INTRODUCTION

Tornado-producing storms occur annually in the Philippine Archipelago; particularly within the Greater Metro Manila Region (GMMR), Western Visayas, and Cotabato provinces. These hazards are by-product from the combination of ample vertical wind shear and atmospheric instability, including lifting mechanism (i.e., forcing) either from plain-to-mountain flow[1] or lowering of the low- and mid-level heights (e.g., mountains, tropical cyclones, easterly waves; Kirshbaum et al. 2018; Capuli 2024a; Capuli et al. 2026, and references therein). Although previous climatological analyses using documented severe weather reports have emphasized the spatial and temporal occurrences of these severe weather events (hereafter SWE; Capuli 2024a), the propensity of these severe convective storms remain poor in the region. Still, the documentation of tornadoes remains serendipitous, occurring typically when tornadoes strike cities amidst the mostly sparsely populated areas (Anderson et al. 2007; Dias 2011; Oliveira et al. 2022).There is evidence, though, that tornadic events in rural lands and forests occur regularly but are rarely reported, especially when the damage is slight or restricted to vegetation with few damage indicators or low population density (Dyer 1988; Wagner et al. 2019; Wurman et al. 2021)[2].

Many studies have addressed the relationship between severe thunderstorms capable of producing tornadoes or tornado outbreaks and associated environmental variables (e.g., Thompson et al. 2012; Lee et al. 2013; Coniglio and Parker 2020; Bagaglini et al. 2021; Pilguj et al. 2022b). This multi-decadal research interest emerged because tornadic storms are among the most devastating natural phenomena, and while local, they cause immense social and material impacts (e.g., Antonescu et al. 2017; Anderson-Frey and Brooks 2021; Púčik et al. 2024). However, limited tornado documentation in the Philippines has left a clear gap in our understanding of the environments and storm characteristics associated with tornadic events (Capuli 2024a). This gap stands in contrast to regions where tornado environments have been more comprehensively

Corresponding author: Generich H. Capuli, genecap89@gmail.com / genhcapuli@rtu.edu.ph / generich.capuli@pagasa.dost.gov.ph

[1] Especially for GMMR and Cotabato provinces as they straddle between two mountainous ranges.

[2] Also known as the Population Density Effect.

described, including the United States (Evans and Doswell 2001; Bunkers et al. 2006; Boustead et al. 2013) and Europe (Groenemeijer and Kühne 2014; Antonescu et al. 2017, 2019). More recently, Mexico has also received increased attention, offering a useful point of comparison given its tropical setting and temporal variation in SWEs (León-Cruz et al. 2022; León-Cruz 2025).

There are key ingredients for severe storm development include: (1) sufficient atmospheric instability, (2) strong vertical wind shear, (3) abundant moisture in both low-levels and boundary layer, and (4) a forcing mechanism to trigger deep moist convection, e.g., an orographic feature, frontal system, dryline, or low-level convergence zone (Rasmussen 2003; Thompson et al. 2003; Mercer et al. 2012; Sherburn and Parker 2014). Furthermore, both Markowski and Richardson (2010) and Davies-Jones (2015) asserted that tornadic thunderstorms that evolve from supercells are more likely to form in environments characterized by high values of convective available potential energy (CAPE) and sufficient deep-layer shear (DLS; refers to the magnitude difference between the wind speeds at the surface and 6 km AGL) which governs the amount of tropospheric instability and mid-level rotation supporting long-lived supercells, respectively (Rasmussen and Blanchard 1998; Brooks et al. 2003; Coffer et al. 2019). However, environments conducive to tornadogenesis are not exclusively limited to the isolated supercells. Some Mesoscale Convective Systems (hereafter MCSs) might produce tornadoes as revealed by observations (Nielsen and Schumacher 2020) and numerical simulations (Nielsen and Schumacher 2018).

To better understand SWEs, it is often necessary to draw on established case studies that have applied similar approaches. Numerous investigations worldwide demonstrate how synoptic-scale and mesoscale environments shape tornado-producing storms. As an example, Thompson and Edwards (2000) analyzed the 3 May 1999 event in the U. S. Great Plains that spawned the Bridge-Creek, Oklahoma tornado, Lopes et al. (2025) documented the 11–12 June 2018 tornado outbreak event in the Argentina-Brazil border, and Choo et al. (2018) examined the 6 May 2012 significant tornado in Japan. All aforementioned authors concluded that tornadic storms can initiate under sufficient or weak synoptic forcing (i.e., frontal systems, upper-level vortices, or jet streaks), favorable combinations of atmospheric instability and vertical wind shear. Moreover, complex topography and mesoscale boundaries, such as orographically-induced lifting and localized outflow or storm interactions (e.g., nudging, merging etc.) can enhance vertical motion and aid in tornadogenesis (Kirshbaum et al. 2018; Nixon et al. 2024). Radar signatures of tornadic supercells have also been examined in recent work, including studies by Clark (2024) and Wakimoto et al. (2025). Through dual-polarimetric parameters such as differential reflectivity (Z_{DR}) and correlation coefficient ratio (CC, also known as ρ_{HV}), these authors have found out the existence of Z_{DR} column within the tornado debris signature (TDS), lowered ρ_{HV}) values (< 0.80) superimposed with high reflectivities. Complimentary research by Yuan et al. (2024) also revealed decreased polarimetric signatures within the low-level mesocyclone of 14 May 2021 Jiangsun tornadic supercell.

Recent efforts to systematically document severe storm phenomena and develop severe storm report databases have begun in the Philippines through Project Severe Weather Archive of the Philippines (SWAP; Capuli 2024a). Still, there is a scarcity of tornado damage surveys that have been conducted. Recent examples of tornado-focused research in the Philippines include those presented by Capuli (2024b) as a thesis, and Capuli et al. (2026). Among these studies, Capuli et al. (2026) described the synoptic and mesoscale conditions (including radar features such as a bounded weak echo region/BWER and hook echo feature) present during the development of a semi-discrete supercell storm that spawned an EF2 tornado in the rural area of Candating in Arayat, Pampanga back on 27 May 2024, located at the favourable area for tornadic storms in GMMR. The authors showed that the tornado developed in a modest synoptic forcing characterized by lowering of 500-hPa mid-level heights as induced by the migratory TC. This synoptic pattern where mid-level height falls are in-place tend to be associated with major tornado outbreaks found in the U. S. Great Plains' Tornado Alley due to the intense and rapid low-level atmospheric response (Mercer et al. 2012; Jiang et al. 2025). The lower troposphere exhibited a moist boundary layer, leading to low lifting condensation levels (LCLs), and sufficient southwesterly windflow (or Southwest Monsoon) that generated ample near-surface and deep-layer wind shear (LLS and DLS) in both speed and direction manifested as a curvature in the hodograph profile. It has been long established that "sickle-shaped" hodographs (or hook shaped; where a layer of strong 0-1 LLS km shear sits beneath an abrupt clockwise turning of the shear vector with height) have become accepted as favorable for significant ($\geqslant$ EF2) tornadoes along cyclonic, right-moving supercells (Weisman and Klemp 1986; Thompson and Edwards 2000; Nixon and Allen 2022), especially those that feature strong shear near the surface (Coffer et al. 2020).

In the early morning hours of 14 September 2025 (in UTC: 13 September 2025), a severe thunderstorm developed over the coastal municipality of Daet, Camarines Norte along ongoing convection associated with an easterly wave. This storm subsequently produced a significant tornado that touched down in and impacted the suburb of Magang, located within the aforementioned municipality. The tornado destroyed several buildings, leaving 121 families (or 605 people) affected after their homes and properties sustained damage. Two fatalities (37-year-old female and a 13-year-old male) were confirmed by the Municipal

Disasters Risk Reduction and Management Office of Daet (MDRRMO-Daet), Department of Social Welfare and Development's Disaster Response Operations Management, Information and Communication (DSWD-DROMIC), and local media. In addition to the Magang tornado, other tornadic events occurred on the same day (two tornadoes and one potential landspout), which are also examined in this study.

Collectively, this localized tornado outbreak; and particularly the Magang event, represents a rare example of tornadic activity in the Philippines as it occurred outside the country's commonly identified tornado hotspots, offering a valuable opportunity to investigate the meteorological processes governing tornado initiation and development in a tropical environment. Although the atmospheric ingredients required for tornadic supercell formation are the same in any part of the world, typical conditions that lead to severe convective storms in this area of the Philippines may exhibit characteristics that differ from their well-documented U. S. Great Plains or European severe storm environments (Taszarek et al. 2020a,b). Thus, an improved documentation of how these ingredients are brought together, in the moist tropical environment of the Philippines, can add to the overall knowledge of the distinct atmospheric regimes that are capable of producing tornadic supercells.

The initial reports and media were scattered across various social platforms, Project SWAP facilitated the systematic collection, verification, and archiving of these materials (particularly in the 4th Data Release). However, given the fact that it occurred just before the sun rises, photographs and videos of the tornado were scarce, but the damage reports were extensive and compiled to form a comprehensive dataset, presented in Section 3, providing essential context for assessing the tornado's impact. This study aims to examine the meteorological conditions that led to tornadogenesis, encompassing the synoptic, mesoscale, and dynamic environmental aspects associated with the parent storm. More importantly, compared to Capuli et al. (2026), a nearby dual-polarization radar was also available at that time (roughly 20 km away from the outbreak) allowing microphysical and refined damage indicator analysis using dual-polarization parameters. Supported by extensive observational data and evaluated through sounding parameters, this investigation serves as a foundational study from which future research in tornadoes that occurred in the tropics can be built.

The paper is organized as follows; Section 2 outlines the materials and methods, including the reanalysis dataset, atmospheric profile parameters, satellite, radar, and lightning data used, in the study. Section 3 presents a comprehensive analysis of the visual-damage, environmental context (from synoptic-scale to mesoscale), and storm dynamics associated with the event. Finally, Section 4 provides the summary of findings and an extended discussion of the results.

2. METHODOLOGY

a. Environmental Reanalysis Dataset

In order to understand the synoptic and mesoscale setting associated with the 13 September 2025 tornado event, this study utilized reanalysis data to assess the potential for SCS development. Reanalysis datasets are widely employed to diagnose atmospheric conditions conducive to severe weather such as tornadoes, damaging winds, and large hail. They are particularly useful for calculating instability indices and other parameters essential to SCS forecasting (Taszarek et al. 2020b).

Environmental reanalysis data for this case were obtained from the fifth-generation European Centre for Medium-Range Weather Forecast (ECMWF) reanalysis (ERA5) accessed through the Climate Data Store (CDS; Hersbach et al. 2020). ERA5 has demonstrated good performance in depicting vertical profiles of convective environments, especially across the United States and Europe (Coffer et al. 2020; Taszarek et al. 2021b; Pilguj et al. 2022a). However, some known biases persist, particularly in the boundary layer. These include discrepancies in low-level parcel characteristics and vertical shear parameters, especially near surface boundaries (King and Kennedy 2019). Such biases are influenced by geographic location and surface elevation. Despite these limitations, ERA5 remains among the most reliable and accessible datasets for investigating severe convective environments, globally (Coffer et al. 2020; Taszarek et al. 2021b,a). For large-scale synoptic analysis, the study domain extended from 4°–22° N latitude and 110°–135° E longitude. The mesoscale sector, which also served for satellite visualization, covered 11°–17° N and 119°–126° E. Both domains used a spatial resolution of 0.25° × 0.25°. An hourly temporal resolution was used to allow detailed analysis of the atmospheric evolution surrounding the event, which occurred around 22 UTC. The time steps selected for in-depth analysis were 21, 22, and 23 UTC, enabling a focused examination of pre-, during, and post-storm conditions.

Although ERA5 provides several convective parameters, including CAPE, it has been shown to substantially underestimate the severity of convective environments, as demonstrated in the hailstorm case study of Capuli (2025). This underestimation is likely related to the ERA5 CAPE formulation, which considers theoretical air parcels originating from multiple model levels below 350-hPa rather than a near-surface parcel. To address this limitation and provide a more physically representative depiction of the convective environment, ERA5 surface and pressure-level fields were combined and re-gridded onto a common grid. CAPE was subsequently recalculated using a most-unstable (MU) parcel defined by near-surface (2 m) parcel

profile. In addition, storm-relative helicity (SRH) was recomputed for the 0–1 km and 0–3 km layers using the fast, publicly available *xcape* codebase (Lepore et al. 2021). Calculations assume a liquid-only pseudoadiabatic ascent, while the storm-relative winds (SRW, represented as V_{SR}) derived from the right-moving storm motion following the Bunkers ID method (B2K; Bunkers et al. 2000).

b. Skew-T Hodograph

Because of the lack of observed proximity sounding (< 30–50 km) in the area of interest, a model-derived profile was extracted from ERA5 data using a combination of single-level and 137 hybrid sigma-pressure level fields. The reanalysis-based soundings were analyzed to assess the thermodynamic and kinematic conditions preceding, at the time, and after the tornadic event.

The parcel profiles were computed assuming a non-entraining, irreversible adiabatic process, following the formulation by Peters et al. (2022c). Compared to the pseudoadiabatic ascent, which assumes all condensate is assumed to fall out of an air parcel immediately (Emanuel 1994), the parcel profile now accounts for the layer of mixed-phase condensate in which liquid and ice are present just below the triple point temperature. This method obeys conservation of energy, instead of conservation of moist entropy, reducing known biases inherent in other parcel models. In fact, Xu and Emanuel (1989) showed that environmental temperature profiles in the tropics more closely align with an adiabatic parcel than pseudoadiabatic, making this approach relevant for analyzing deep convection in the tropics.

Furthermore, an irreversible adiabatic ascent with entrainment was also employed to compute the Entraining CAPE (ECAPE; Peters et al. 2023). ECAPE accounts for dilution of updraft plumes due to environmental entrainment, particularly under conditions of limited storm-relative inflow and/or mid- to upper-tropospheric dryness. Thus, providing a more realistic estimate of updraft intensity than the conventional, undiluted CAPE, which can overestimate buoyancy in environments where entrainment is significant. All undiluted buoyancy profiles are calculated using virtual temperature correction. Depending on meteorological context, either MU or surface-based (SB) parcels were selected for key thermodynamic parameters. CAPE and the level of free convection (LFC) were computed using MU parcel profiles, while convective inhibition (CIN) and lifted condensation level (LCL) were determined using SB profiles. Although mixed-layer parcels are often preferred for their robustness, SB and MU parcels were preferred in this study due to their better representation of near-surface instability (or stability) and lowest cloud base heights. These factors are critical in distinguishing surface-based from elevated convection, particularly in tornadic environments.

The hodograph was used to understand the kinematic properties associated with the tornado event. In a conventional, ground-relative hodograph, there is no transformation is made to the modeled u and v wind components (Markowski et al. 2003; Nowotarski and Jones 2018). However, this method cannot capture how the wind profile changes from the perspective of the storm or assess for diagnosing convective storm dynamics. To address this, the study uses the storm-relative hodograph (SR hodograph), a novel analytical approach recently introduced by Capuli et al. (2026). This was done by subtracting the estimated storm motion calculated using the B2K method, also an important component of ECAPE, from the modeled wind profile. The resulting V_{SR} was then analyzed based on assumptions regarding storm motion. Due to the absence of observational constraints such as storm motions as derived from radar, supercell type, or storm mode, the right-moving vector ($B2K_{RM}$) was assumed, consistent with standard practice for the Northern Hemisphere. This assumes that the storm moves to the right of the non-pressure-weighted mean wind.

The kinematic parameters were calculated from the interpolated model output of the u and v wind components. The bulk wind difference (BWD) was calculated across several vertical layers to assess shear magnitude. These included the layers from 0–500 m (BWD_{500}), 0–1 km (BWD_{01}), 0–3 km (BWD_{03}), 0–6 km (BWD_{06}; DLS), 1–3 km (BWD_{13}), and 1–6 km (BWD_{16}). SRH, represented by the vertically integrated storm-relative flux of streamwise vorticity into an updraft, is of the greatest dynamical importance in this regard (Davies-Jones 1984). The SRH was computed for several layers: 0–500 m (SRH_{500}), 0–1 km (SRH_{01}), 0–3 km (SRH_{03}), and 1–3 km (SRH_{13}). For the near-ground layer (0–1 km), the mean V_{SR} was calculated relative to the $B2K_{RM}$. This analysis also included the mean streamwise vorticity integrated over 0–500 m and 0–1 km layer denoted as ω_{s500}, and ω_{s500}, respectively. These quantities were calculated as:

$$\omega_s = \frac{\nabla \times (v - c) \cdot (v - c)}{||(v - c)||}$$

where v is the three-dimensional environmental wind and c is the storm motion vector under the assumption of the B2K method. Furthermore, the vertical vorticity along the low-level mesocyclone was calculated. Based on the first-order approximation of tilting efficiency proposed Coffer et al. (2023), the horizontal vorticity generated from the tilting of streamwise vorticity in a purely streamwise environment can be expressed as;

$$\zeta_{\mathrm{LLM}} = \omega_s \frac{w}{V_{\mathrm{SR}}}$$

where ω_s is the streamwise vorticity[3], w is the vertical velocity of the updraft[4], and V_{SR} is the storm-relative wind in the lowest 1 km. This formulation highlights how the conversion of environmental streamwise vorticity into vertical vorticity depends on the interaction and balance between vertical and horizontal motions (Davies-Jones 1984). It provides a physically intuitive approximation for assessing the potential for mesocyclone development and subsequent tornadogenesis.

Other kinematic parameters were also evaluated to characterize storm dynamics. The "critical angle" (CA), which describes the angle between the storm inflow and the shear vector in lowest kilometer, was calculated using the method proposed by Esterheld and Giuliano (2008). The "streamwiseness" ($\widetilde{\omega_s}$) of horizontal vorticity was also calculated by dividing the integrated streamwise component of horizontal vorticity by the integrated total magnitude of the horizontal vorticity in a given layer;

$$\widetilde{\omega_s} = \frac{\omega_s}{\omega}$$

The use of $\widetilde{\omega_s}$ is justified for two reasons. First, near-zero shear conditions are rare in tornado environments (Coffer et al. 2020). Second, the parameter offers intuitive interpretation; for example, a value of 0.9 indicates 90% of the horizontal vorticity is streamwise in nature. Nonetheless, the degree to which vorticity is streamwise remains a fundamental aspect of supercell dynamics and tornadogenesis (Coffer and Parker 2017).

Lastly, the Deviant Tornado Motion (DTM) was calculated based on the method developed by Nixon and Allen (2021). This parameter evaluates the potential deviation of tornado motion from both the low-level advective flow and the parent storm motion, and offers insight into tornado track behavior relative to ambient wind conditions. All reanalysis-derived soundings associated in this event were analyzed using SounderPy by Gillett (2025). A list of the evaluated kinematic and thermodynamic parameters, along with their definitions and computation methods, is presented in Table 1.

c. Satellite Data

1) HIMAWARI-9 Satellite Data

High spatio-temporal resolution data from the Advance Himawari Imager (AHI) aboard the HIMAWARI-9 satellite (Bessho et al. 2016) were used to identify and characterize the convective system associated with the tornadic event. HIMAWARI-9 comprises of 3 VIS bands (central λ ranging from 0.47 μm–0.64 μm), 3 NIR bands (central λ ranging from 0.86 μm–2.3 μm), and 10 IR bands (central λ ranging from 3.9 μm–13.3 μm). Particularly, this study selected the visible bands and the 10.4 μm infrared) atmospheric window band (Band 13; B13) to monitor deep convection. B13 is particularly useful for detecting cold cloud-top regions [i.e., Brightness Temperature (BT) < 235 K (–40 °C)] while minimizing interference from water vapor (Hirose et al. 2019). It is also widely adopted for rapid identification of convective features associated with extreme rain events with small lag time Wang et al. (2022). The visible bands have spatial resolution ranging from 500 m–1 km, while B13 has a coarser resolution of 2 km.

Penetrative overshooting tops (OT) were also examined as signatures of severe convection. OTs are identified as local minima in cloud-top brightness temperature (BT < –60–65 °C) and signify strong updrafts capable of reaching above the equilibrium level (EL) and into the lower stratosphere. Their occurrence is frequently linked to intense strom dynamics and severe weather, including large hail and tornadoes (Bedka et al. 2010). Aside from identifying OTs, the associated convective system scale i.e., area is also distinguished in this study. This is by setting an IR threshold of –40 °C and identifying the radius (km) of a circle with the same area as covered by the image pixels composing the convective storm;

$$r = \sqrt{N\left(\frac{A}{\pi}\right)}$$

where N is the number of pixels and A is the area of the pixel. As a rule-of-thumb, MCS are defined as convective systems with radii ¿ 100 km, mean cloud temperature ¡ –30 °C for the entire convective system, and with at least one overshooting top (< –65 °C; Carvalho and Jones 2001). Meanwhile, smaller convective storms that fall between 50 and 100 km and have cloud temperatures < –30 °C are categorized as weak and disorganized convective systems (WDCSs). The WDCS are the most frequent convective system in the Tropics (Rossow et al. 2013; Tan et al. 2013).

2) PlanetScope Observations

Remote sensing provides innovative technologies for assessing tornado debris (Hoque et al. 2017). These technologies have shown to be effective in damage assessment following disasters, as demonstrated by numerous research (Xie et al. 2016). Aerial images (Schaefer et al. 2020), a form of airborne remote sensing technology, are one important source of data for storm damage assessment.

PlanetScope (PS) is a CubeSat 3U form factor (10 cm × 10 cm × 30 cm) satellite constellation operated by Planet Labs, Inc. and was utilized in this study. While in sun-synchronous orbit, these cubesats provide daily 4-band (RGB and NIR) imagery of the Earth at 3-m spatial resolution (Planet Team 2024). Currently in orbit are the Dove Classics, the improved Dove-Rs with more spectral and radiometric precision and sharpness, and the hyperspectral

[3] In this case, angle-average and its maximum ω_s in the lowest 1 km.

[4] Here, $CAPE_{03}$ is used as a proxy for low-level updraft strength, with $w = \sqrt{2CAPE_{03}}$ assuming negligible entrainment and parcel dilution.

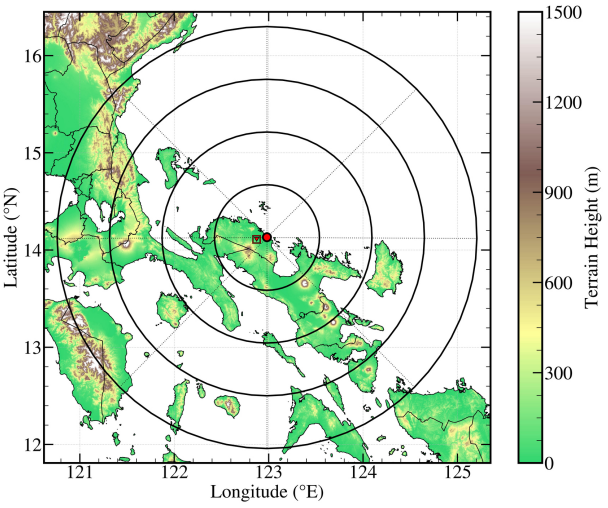


Figure 1. Elevation map encompassing S-DAT (red circle) and its 240 km radar coverage with increments of 60 km each. The red triangle enclosed by a box is the location of the tornado outbreak event

SuperDoves. Most images used in the study were daily Dove Classic imagery, or the newer generation Dove-R images (https://www.planet.com/). These have a Ground Sampling Distance (GSD) of 3–4 m at nadir and a positional accuracy of < 10 m RMSE. We used the level 3B Surface Reflectance (SR) product, which is orthorectified and atmospherically corrected by Planet Labs with their in-house processing. These provide more consistency across time and location localized atmospheric conditions while minimizing uncertainty in the spectral response.

The high-resolution satellite images that were chosen for this analysis are nearly clear images (cloudless, hazeless, and smokeless) within the areas of interest for this analysis of before (04 August 2025)[5] and after the event (28 September 2025). Upon inspecting the raw data along the investigation area, it contains some thin-to-thick clouds. Therefore, we apply spatial masking using a sensor-agnostic deep learning model that segments clouds and cloud shadow. This is applied through OmniCloudMask (OCM; Wright et al. 2024), a python library that consists of two ensembled U-Net models (Ronneberger et al. 2015). These constituent models leverage the use of Fastai Dynamic U-Net (Howard and Gugger 2020), which allows any CNN to be used as a backbone model. The models chosen for this purpose were the *"RegnetY 004"* and the *"ConvNextV2 nano"*, supplied with pretrained weights sourced from the timm library (Wightman 2019). With the masked data, the PS satellite imagery can be used to detect the damage from a tornado event using Normalized Difference Vegetation Index (NDVI).

[5]Typically, it is better to attain a pre-event imagery in the same month i.e., in September, but observations for it were heavily obscured by clouds.

Bandwidth	S-band
Polarization	Dual-Polarization (Dual-pol)
Position	14.128°N, 122.982°E
Altitude	34 masl
Pulse Width/Maximum Range	~0.001 ms / 240 km
Beam width/Range resolution	1.68° (h and v) / 250 m
Pulse Repetition Timing (PRF)	0.001 s (599.88 Hz)
Nyquist Velocity	63 m s^{-1}
Number of Elevation Angles	14
Elevation Angles	0.5°, 1.5°, 2.4°, 3.4°, 4.3°, 5.3°, 6.2°, 7.5°, 8.7°, 10°, 12°, 14°, 16.7°, 19.5°
Volume Cycle Interval	10 minutes
Start of operation	2018

Table 1. Technical specifications of Daet Radar (S-DAT).

Following the creation of the before and after from the PS with clouds removed, the NDVI value is calculated using the pre-tornado imagery ($NDVI_{BEFORE}$), as well as using the post tornado imagery ($NDVI_{AFTER}$). These values are then used to measure the percent change in NDVI between the before and after images. This normalized percent change is an empirical method of calculating the change in plant health and accounts for the starting health of the vegetation. Previous studies used the difference between the two NDVI images rather than the percent change equation due to the similarity in vegetation conditions as they analyzed singular events. Burow et al. (2020) took the NDVI values from post event imagery and subtracted them from the pre-event imagery of three long-track tornadoes' damage path to create an NDVI difference image.

The normalized percent change in NDVI value is calculated as;

$$NDVI_{\text{CHANGE}} = \frac{NDVI_{\text{AFTER}} - NDVI_{\text{BEFORE}}}{NDVI_{\text{BEFORE}}} \times 100\%$$

d. Observational Data from DOST-PAGASA

1) Radar Data

DOST-PAGASA operates a nationwide network of 17 weather radars, 7 of which are dual-polarization (dual-pol) C-band radars, 3 dual-pol S-band, and 7 single-polarization (single-pol) S-band radars. These systems support the agency's capacity for early detection and monitoring of weather systems across the archipelago. The 13 September 2025 tornadic supercell tracked through the domains of the Daet S-band radar (hereafter S-DAT), a dual-polarization radar strategically located on near the coast of Daet, Camarines Norte (14.128562 °N, 122.982693 °E); along the Bicol Region (Fig. 1). The S-DAT radar, which operationally started by 2018, provides extensive coverage over this region, an area that typically sees tropical cyclone activity. S-DAT employs a Modified Volume Coverage Pattern 11 (VCP11) which optimizes radar sampling across

both low and high elevation angles. This configuration is particularly well-suited to tropical environments. For this study, the Doppler mode scanning radius was set to 240 km. Technical radar specifications are described in Table 2.

S-DAT's radar data underwent quality control based on a fuzzy logic approach designed to detect and eliminate interference patterns. This method draws on prior algorithm assessments (e.g., Kilambi et al. 2018; Overeem et al. 2020, and references therein) and was adapted for both single and dual-pol radar products following the framework described in Lin et al. (2021). To correct for velocity folding in the radial velocity (V_R) data, a regional dealiasing technique was implemented using the Python ARM Radar Toolkit (PyART; Helmus and Collis 2016). Following the procedures outlined by Capuli et al. (2026), the *dealias region based* module was applied to identify coherent velocity regions, which were iteratively unfolded via dynamic network reduction methods based on local standard deviations. Specifically, we perform a two-stage dealiasing and composite reconstruction of the radial velocity by identifying tornadic and non-tornadic signatures. A velocity texture field was derived using the *calculate velocity texture* function, representing the V_R's standard deviation. Regions with low velocity texture values (< 5 m s^{-1}) were masked, and initial dealiasing of the entire velocity field was performed to obtain a smooth, coherent non-tornadic velocity background. The tornadic signature was then isolated using a simple gate filter that excluded reflectivity (Z_H) values < 40 dBZ. A second dealiasing process was subsequently applied to these isolated regions, followed by an additional correction step using the *dealias unwrap phase* module to remove residual artifacts introduced by the region-based dealiasing. Finally, the non-tornadic and tornadic dealiased velocity fields were merged into a composite dealiased velocity product, achieved by masking invalid or missing values in the non-tornadic field and replacing them with corresponding values from the tornadic field.

To identify potential rotation signatures within the dealiased V_R field of the S-DAT radar, we used the Mesocyclone Detection Algorithm (MDA) and its detection thresholds as developed by Stumpf et al. (1998) and following modern applications of this MDA stipulated in Hengstebeck et al. (2018) and Feldmann et al. (2021). These parameters involved the maximum tangential (rotational) velocity (> 10 m s^{-1}), vorticity ($> 10^{-2}$ s^{-1}), horizontal scale, and duration of the feature. In particular, the rotational velocity (per nomenclature; V_{rot}) is calculated using the maximum outbound velocity ($V_{max,out}$) and the maximum inbound velocity ($V_{max,in}$) determined from the radial segments in the 2D feature;

$$V_{rot} = \frac{V_{max,out} - V_{max,in}}{2}$$

The vertical vorticity, as measured through the radar (ζ_{rad}), can be determined using the equation below;

$$\zeta_{rad} = 2\frac{V_{max,out} - V_{max,in}}{\Delta X}$$

where ΔX is the cartesian distance (m) between the velocity maxima.

While we apply these mesocyclone detection techniques and thresholds, we must assert that these variables are largely adapted from studies conducted in mid-latitude regions, where radar configurations, storm structures, and environmental conditions differ substantially from those in the tropics. Therefore, we encourage future readers (and more importantly, Filipino meteorologists who wanted to dive in severe weather meteorology) to develop more robust and regionally calibrated detection algorithms suited to the broader Philippine radar network such as conducted by Feldmann et al. (2021) for the Alpine region.

Lastly, the vertical velocity (w) was retrieved based on the dealiased V_R and reflectivity. A commonly used technique for this approach is the terminal velocity-reflectivity method (V_T-Z_H; e.g., Atlas et al. 1973), which is reflectivity-weighted by employing an empirical power-law relationship between Z_H and V_T;

$$V_T = aZ_H^b \left(\frac{\rho_o}{\rho}\right)^{0.4}$$

$$w = V_R - V_T$$

with $a = -2.65$ and $b = 0.114$, where V_T is in m s^{-1}, Z_H is reflectivity in mm^6 m^{-3}, $\rho_0 = 1.225 \times 10^{-3}$ g cm^{-3}, and ρ is derived from an ERA5 model sounding (at 22 UTC). The relationship is meant for liquid drops and is not applicable at the melting level due to bright banding or above the freezing level for frozen precipitation. Considerations are required for using the V_T-Z_H method to estimate V_T introduces uncertainty into the retrieved w observations. Such as this is only accurate to within 1 m s^{-1} for Z_H ¡ 40 dBZ (Atlas et al. 1973). The increased uncertainty is due to the wide range of rain drop size distributions (DSD) producing low Z_H, from a large number of small drops (e.g., drizzle) to a small number of large drops at the edge of a convective storm.

Lastly, given the radar's bandwidth at S-band and being well-maintained by DOST-PAGASA's radar operators, specific attenuation correction (including other correction factors such as for systematic biases and Wet Radome Effect etc.) were not performed as S-band's attenuation is vanishingly small (Diederich et al. 2015).

2) Lightning Data

Lightning data was obtained from DOST-PAGASA Lightning Detection Network (PLDN), which consists of 28 strategically deployed lightning sensors distributed

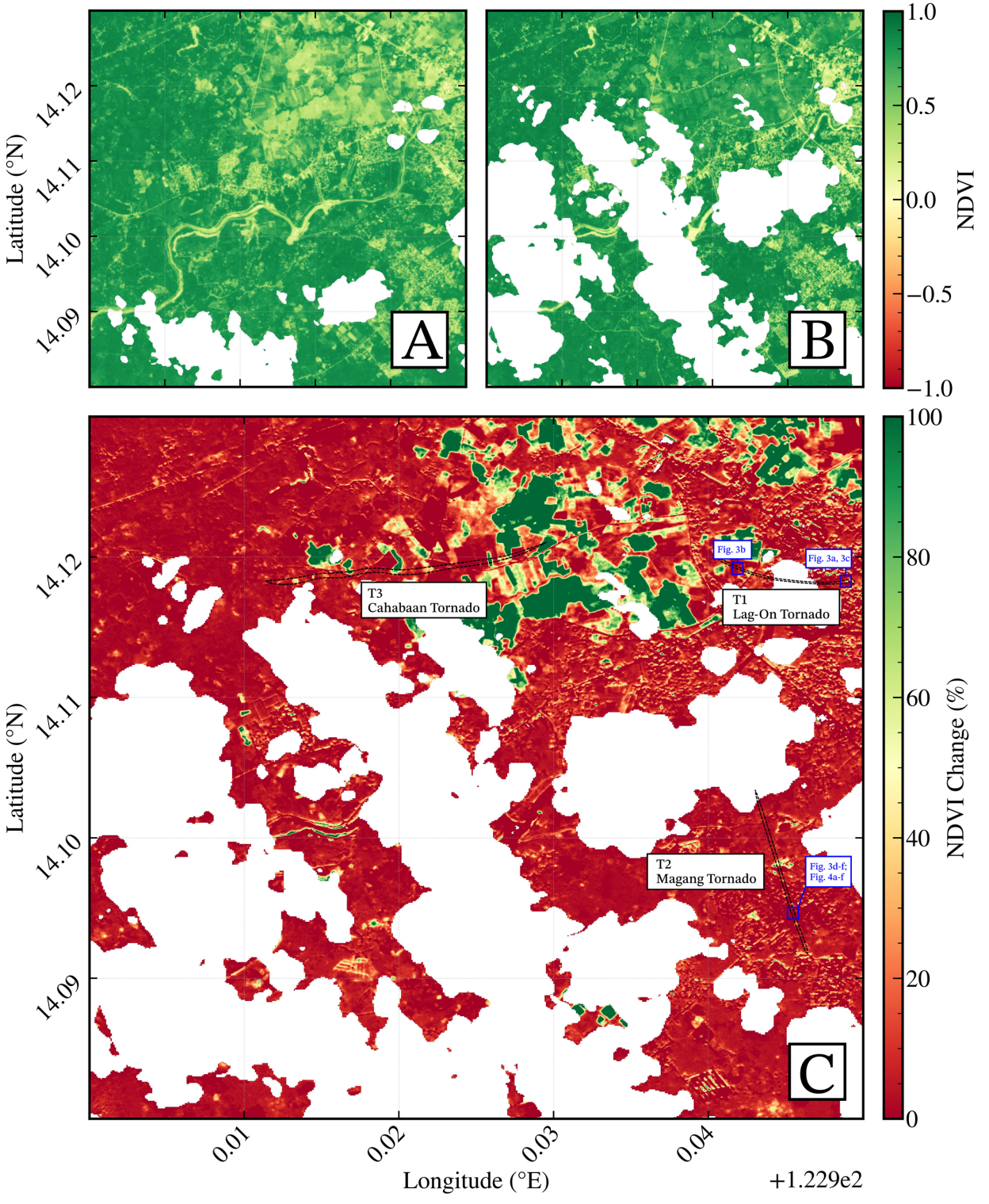


Figure 2. Isopleths of delineated tornado tracks based on PlanetScope observations. (a) $NDVI_{BEFORE}$ at 04 August 2025, and (b) $NDVI_{AFTER}$ at 28 September 2025, and (c) $NDVI_{CHANGE}$ between 04 August and 28 September 2025. For Panel C, the tornado tracks (black dashed lines) are labelled accordingly. Blue boxes correspond to the identified damage indicators and visual observations of the tornadoes.

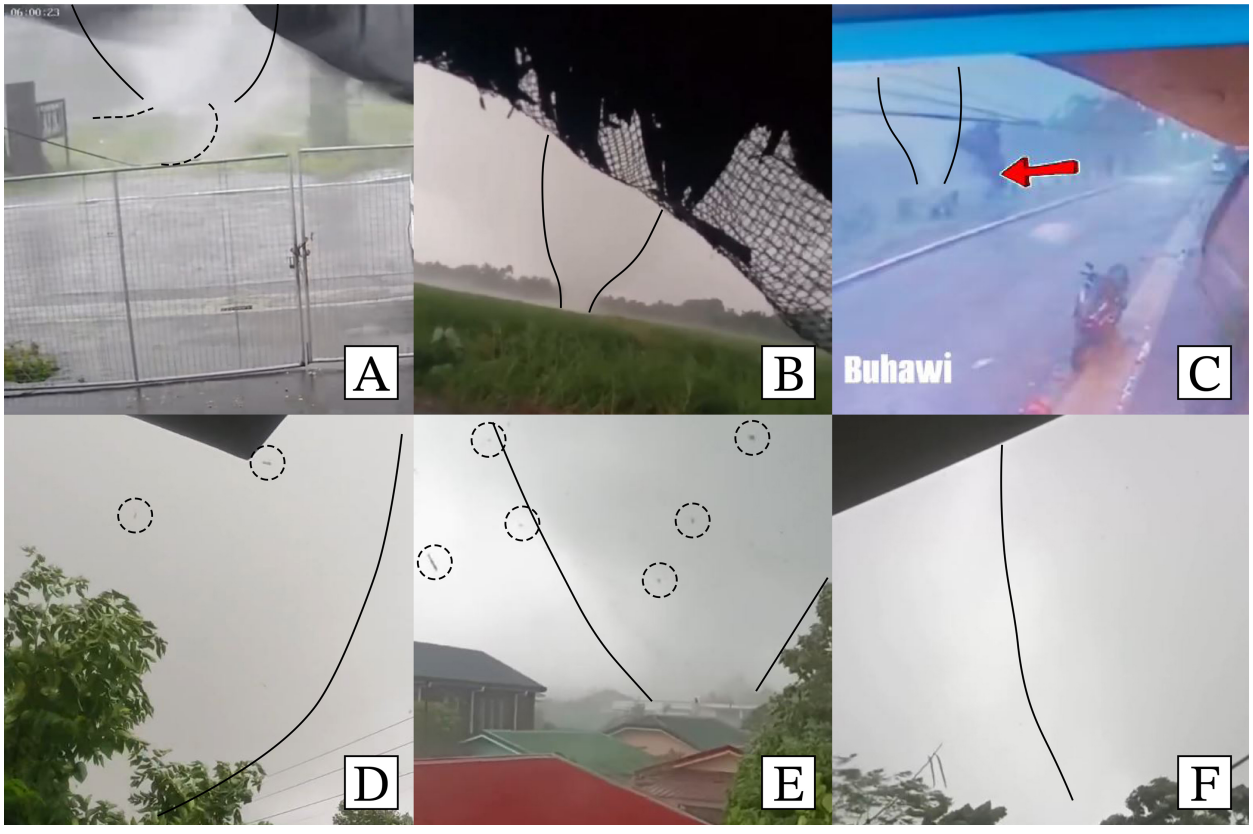


Figure 3. Video surveillance of T1 and T2 (as labelled in Figure 2) that impacted Brgy. Lag-on and Magang in Daet, Camarines Norte. Courtesy of (a) Dong Medina Dela Cruz, (b) Vivian Clavite, (c) Marcelyn Centeno Carillo, (d) Wilson Obog Pajares, (e) Albert Elnar Tagolino, and (f) Chai Gallardo. Dashed circles in 4d and 4f are debris lofted by T2-Magang Tornado.

throughout the country. These sensors are primarily located within PAGASA observing stations and support real-time thunderstorm monitoring. Since its operational inception in 2018, the PLDN has provided continuous coverage for both intra-cloud (IC) and cloud-to-ground (CG) lightning discharges. It also enables early detection of rapid increases in lightning activity, known as 'lightning jumps', which often precede the onset of severe weather (Schultz et al. 2011). For this case study, lightning data spanning from 21 UTC of 13 September 2025 to 00 UTC of 14 September 2025 were used.

To ensure data quality, all lightning strokes were aggregated into 1-minute intervals. For each interval, we calculated the total number of strokes, along with average and median peak current values, separately for positive and negative polarities. This time-resolved approach enabled a detailed characterization of lightning intensity, polarity distribution, and temporal evolution in relation to the supercell's development and maturity.

3. RESULTS AND DISCUSSION

a. Tornado Damage Paths and Visual Observations

The damage paths of the tornadoes that struck several areas of Camarines Norte were identified through change detection analysis using pre- and post-event PlanetScope observations. Figure 2 illustrates the NDVI values before and after the event, as well as their difference. In this study area, it mainly consists of land cover types of rural settings, including bare soil, residential structures, paved surfaces, and vegetation.

Each isopleth (black dashed lines) was labeled according to its associated tornado signature (e.g., TOR1, TOR2, etc.). TOR1 corresponds to the Lag-On tornado, which was supported by multiple eyewitness accounts confirming a tornado on-the-ground, as documented in Figure 3a-c. TOR2 corresponds to the well-documented Magang tornado, characterized by a clearly vortex and defined damage swath across the Fairview 2 area of Magang, Daet, as shown in Figures 3d-f and 4, respectively. In addition, a third damage track, designated as TOR3, was identified and attributed to the Cahabaan tornado. Unlike the preceding cases, this event was not reported in official records

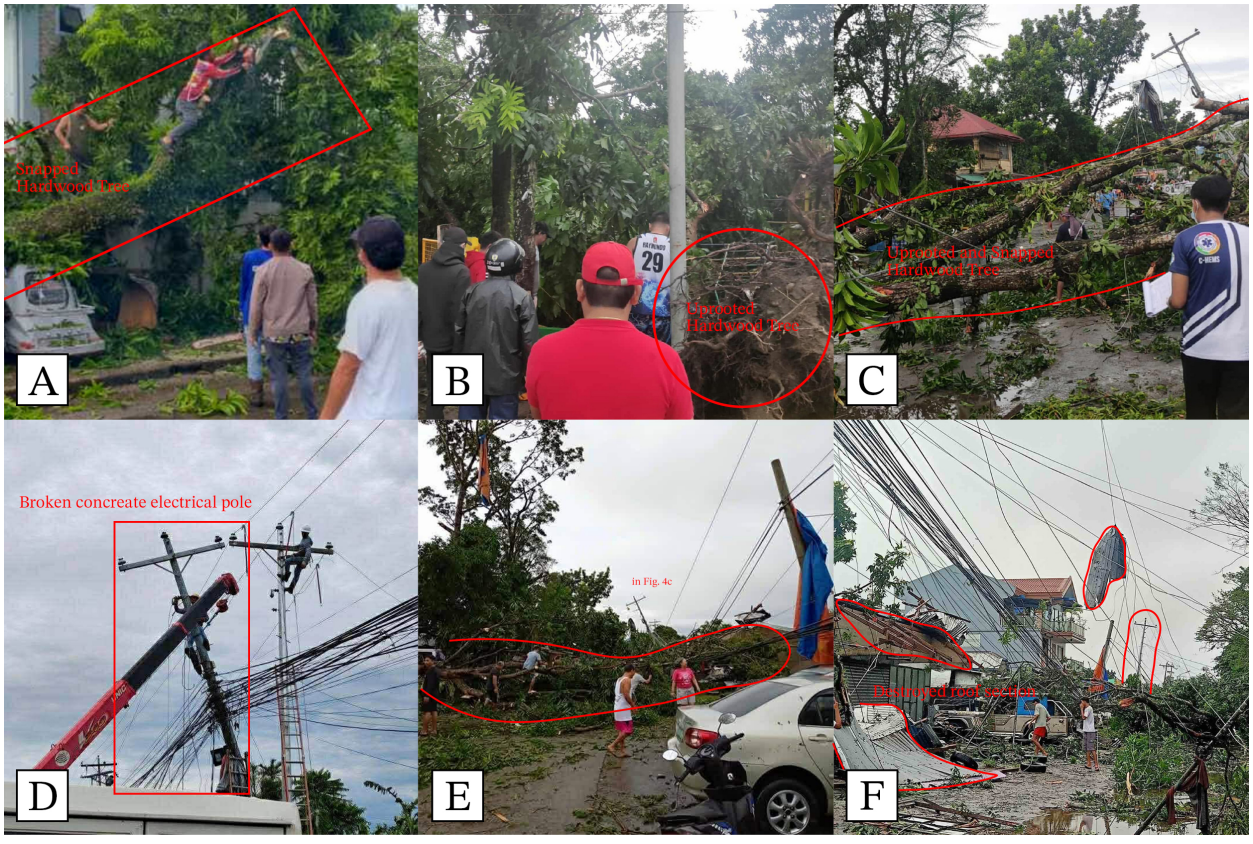


Figure 4. Ground photos of the damages brought by T2 (as labelled in Figure 2; otherwise known as the Magang event).

nor widely documented across online platforms, including social and news media. Nevertheless, three distinct vortex paths were discerned through careful examination of available damage imagery and supporting radar analysis, particularly for TOR3, as discussed in a subsequent section. Furthermore, two additional features were identified: TOR4, corresponding to the Napilihan tornado, and TOR5, representing a small vortex signature likely associated with a non-supercellular landspout. These classifications are supported by radar-based analyses presented later in the study.

As shown in Fig. 2c, which represents the difference between the two image acquisition dates, TOR1 exhibits a well-defined, east–west elongated swath marked by a pronounced change in NDVI, consistent with the inferred tornado track. The path appears to originate near Lag-On and extends into adjacent rice and crop fields, with maximum NDVI change reaching ~82–85%. In contrast, TOR2 displays a southeast–northwest-oriented damage swath, with peak NDVI changes approaching ~90% along its trajectory. This path originates over agricultural fields and extends toward the more densely populated area of Magang. Similarly, TOR3 presents a generally east–west-oriented damage zone, characterized by multiple patches of substantial NDVI change exceeding 90–100%. However, portions of this signal may be affected by the relatively large temporal gap between acquisition dates, introducing potential contamination. Furthermore, TOR1 produced a damage track approximately 1 km in length, while TOR2 extended to about ~2.5 km, and TOR3 reached ~3.2 km. Focusing on TOR2 (Magang Tornado), the damage survey along this track indicates impacts to a range of structures, including one- to two-story residential homes, several electrical transmission lines, a church, and a junior/senior high school building. The nature and severity of these damages are consistent with the International Fujita (IF) Scale criteria for IF2–IF2.5 intensity rating, based on the corresponding Damage Indicators (DI) and Degrees of Damage (DoD) observed across multiple locations, in classical terms the intensity can reach up to EF3 in the Enhanced Fujita (EF) scale. Briefly, the IF Scale was developed by European Severe Storms Laboratory (ESSL) that utilizes instantaneous three-dimensional winds at the height of the damage instead of a 3-s-averaged horizontal wind at 10 mAGL (Groenemeijer et al. 2023), and was adopted to this study for damage identification.

To support the IF2.5 classification of the Magang tornado, a comprehensive damage survey was conducted us-

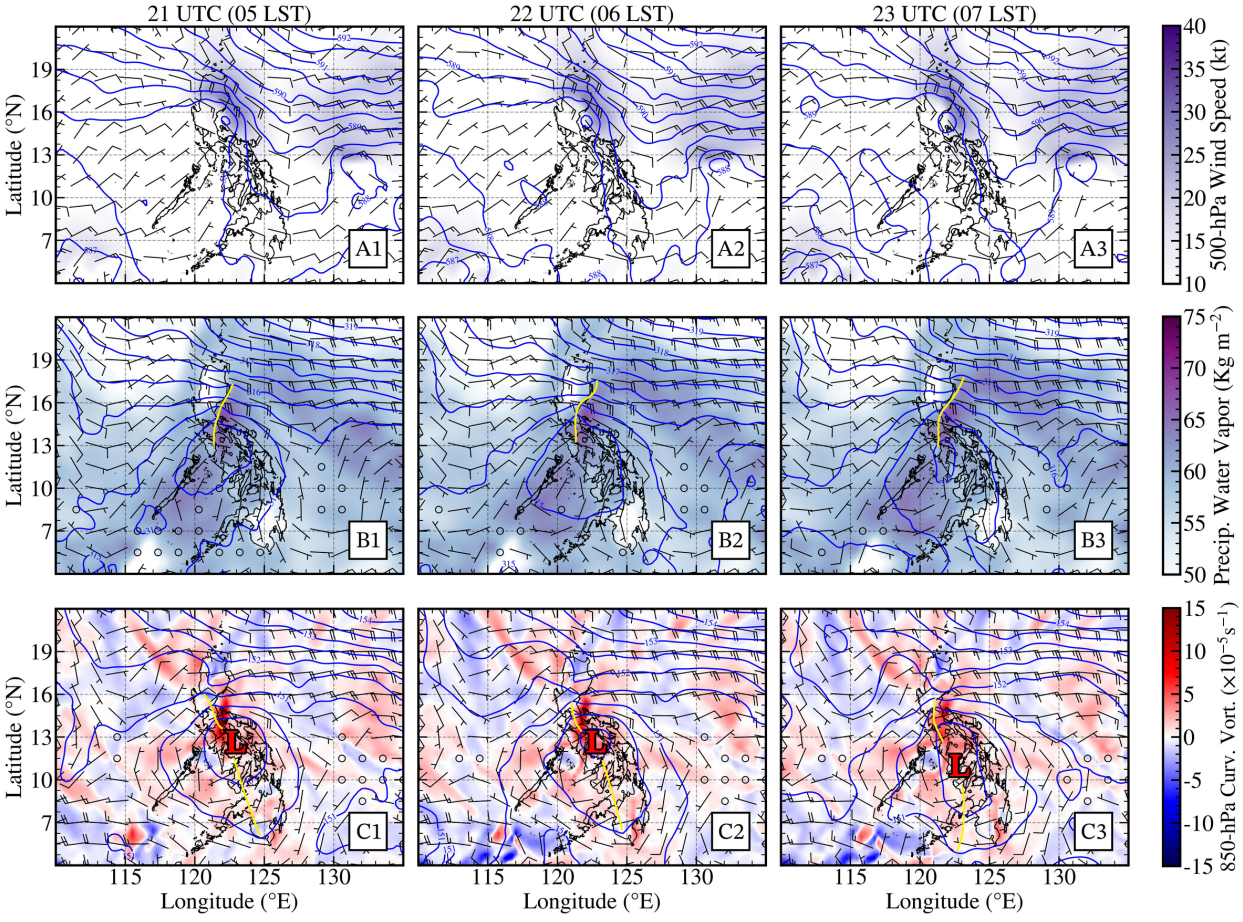


Figure 5. Synoptic environment of the Philippine archipelago before (1; 21 UTC/05 LST), during (2; 22 UTC/06 LST), and after (3; 23 UTC/07 LST) the event. (a) 500-hPa Geopotential heights (blue; dam) and winds (kt). Contours are wind speeds > 10 kts. (b) 700-hPa Geopotential heights (blue; dam), precipitable water vapor > 50 kg m^{-2} (contour), and winds (kt). (c) 850-hPa Geopotential heights (blue; dam), curvature vorticity (× 10^{-5} s^{-1}), and winds (kt). Yellow lines correspond to the axis of the inverted trough.

ing the International Fujita (IF) scale framework, focusing on the most severe structural and environmental impacts observed in the field. Aside from Figure 4 depiction, several indicators reached or exceeded the IF2 threshold, corresponding to estimated wind speeds of at least 60 m s^{-1} (220 km h^{-1}) attached to the supplementary document of this study. Notably, the snapping of large, strong trees (TR-S, DoD 5) was a recurring indicator of high-intensity winds, as seen in the vegetation surrounding public transport and private vehicles (Figs. 4a, 4c, 4f-unhighlighted, S2, S3, S5, S9, and S10). One of the most critical observations involved a large tree uprooting (TR-S, DoD 3) that resulted in two casualties; this specific instance was adjusted to an IF2 rating to reflect the localized intensity of the vortex (Fig. 4b & S6). Structural evidence further corroborated these high wind estimates, particularly regarding engineered roofing systems. Analysis of building indicators (BR-D, DoD 2) revealed instances where strong roof structures were completely blown over or destroyed, consistent with wind speeds ¿ 60 m s^{-1} (Fig. 4f, S2, S11). Additionally, the overturning of three-wheeled public transport vehicles (VH-C, DoD 2) provided a clear mobile indicator of IF2 intensity. The highest intensity recorded during the survey involved a strong, well-rooted tree that was snapped and stripped of its branches (TR-S, DoD 5); given the degree of debranching and the sturdiness of the specimen, this indicator was adjusted to IF2.5, substantiating the peak classification for this event (Fig. S16). Supplementary photographs of the affected structures are georeferenced across the damage path of TOR2 shown in Fig. 2c. Notably, the spatial distribution of observed damages corresponds closely with in situ photographs provided by local residents. This alignment reinforces the reliability of the damage path delineation and further substantiates the IF2.5 (approx. EF3) tornado classification for this event. Meanwhile, TOR1 and TOR5 were assigned IF0 ratings (EF0-equivalent), as these brief events were largely confined to open terrain, resulting in no observable damage

and no reports from nearby residents. In contrast, TOR3 and TOR4 were assigned IF1 ratings (EF1-equivalent), based on radar-derived signatures presented in subsequent analysis.

b. Synoptic Conditions

To investigate the mechanism that facilitated convective initiation, we analyzed the synoptic environment using multiple constant-pressure levels, as illustrated in Figure 5. At 500-hPa (Fig. 5a1–a3), thorough inspection reveals a mid-level height perturbation along the eastern coast of mainland Luzon with 15–25 kts southeasterly winds rounding the base of the mid-level feature. Unlike the EF2 tornado that tore the town of Candating, Arayat back on 27 May 2024 (Capuli et al. 2026), the 'isohypses' did not change i.e., lowered to induce subtle mid-level forcing for ascent, but rather the upstream/upward flow may have provided persistent ascent and moisture transport, which in turn can promote atmospheric destabilization. Regardless of whether the mid-level perturbation appeared relatively weak, it favored discrete cell development of convective cells (Schumann and Roebber 2010). Whereas a stronger synoptic typically supports mixed or linear convective modes e.g., quasi-linear convective systems (QLCS; Bunkers et al. 2006; Dial et al. 2010)[6].

At 700-hPa (Fig. 5b1–b3), the height perturbation becomes more pronounced (yellow line), exhibiting a relatively broad center over the Visayas region. This perturbation likely reflects the low-level easterly trough axis and is accompanied by precipitable water (PWAT) values > 60 kg m^{-2} during the analysis period, indicating a deeply moist lower troposphere. This supports the results of Serra et al. (2008) who found that these perturbation waves in the tropics are accompanied by warm, moist low-levels due to adiabatic barotropic and baroclinic conversions to eddy energy. Such moisture availability is a critical ingredient for the initiation and maintenance of convective updrafts, including those associated with supercells (Púčik et al. 2015; Rasmussen et al. 2020). Winds at this level were predominantly southeasterly to easterly, consistent with the mid-level flow, suggesting the presence of modest vertical speed shear.

Complementing the 700-hPa analysis, the 850-hPa fields (Fig. 5c1–c3), representative of the planetary boundary layer, reveal a tropical easterly wave characterized by an elongated low-pressure system (circulation center marked by a red "L"), with its wave axis extending from Central Luzon to Mindanao. The easterly inverted trough is identified using 850-hPa curvature vorticity (ζ_{CV}), a component of relative vorticity, where enhanced positive ζ_{CV}) (> 1.0 × 10^{-5} s^{-1}; Brannan and Martin 2019; Elless and Torn 2019) along the base of the open wave indicates low-level cyclonic circulation over the area of interest. Serra et al. (2008) further noted that the convective maximum in such low-pressure systems is typically located behind (i.e., upstream of) the trough axis. In this case, the collocation of the vorticity maximum, modest moisture advection, and sufficiently high PWAT values suggests that the tilted structure of the tropical wave promoted low-level convergence over eastern Luzon. Therefore, large-scale advective processes associated with the tropical wave and its trough axis likely played a crucial role in establishing an environment favorable for severe thunderstorm initiation, including supercells capable of tornadogenesis (Doswell and Bosart 2001).

Several dynamic cross sections across the regions of interest are shown in Figure 6 at 22 UTC (06 LST). In particular, negative values of the convergence ($\nabla F < 0$) are found in the low-levels up to mid-levels (500-hPa) in Figure 6a are indicative of forcing for ascent is still present in the environment especially along the upstream section of the inverted trough. This was complemented by negative vertical velocity anomalies reaching ~–0.3–0.5 Pa s^{-1} in the lower troposphere, particularly between 800 to 300-hPa pressure levels (Fig. 6b). These upward vertical motions serve as an important ingredient for initiation and sustaining deep convective storms and its updrafts (Wakimoto et al. 2004). These dynamical and synoptic processes may have been further modulated by local topography via thermal winds i.e., slope and mountain-induced circulations, given the proximity of the outbreak sequence in the Camarines Norte Mountain Range (> 300 mASL) with the highest being Mt. Labo (~1,500 mASL) and elevated terrain of Bicol Natural Park and its Mt. Balagbag (~1,000 mASL) to the west and south of Daet, Camarines Norte, respectively. Such orographic influence may have caused the enhancement of convergence and vorticity as southeasterly-to-easterly winds impinged on the windward slopes of higher terrain, enhancing low-level confluence and horizontal shear along the foothills and coastal plain near the area of interest, thus promoting lifting of warm, moist air parcels and initiating deep convection capable of tornadogenesis (Kirshbaum et al. 2018). We discuss further this terrain enhancement feature in the subsequent section.

c. Mesoscale Environment

Analyzing the atmospheric conditions during the early morning hours is essential for understanding the background environment that influenced storm development. The mesoscale convective conditions are illustrated in Figure 7 using ERA5 reanalysis from 21–23 UTC (05–07 LST).

As shown in Figures 7a1–a3, CAPE measurements between 1500–2000 J kg^{-1} were present in the area of interest

[6]The Oklahoma–Kansas tornado outbreak of 3 May 1999 was an example of weak-ill defined forcing (Thompson and Edwards 2000). QLCS is a subset of MCS and is synonymous to a Squall Line system.

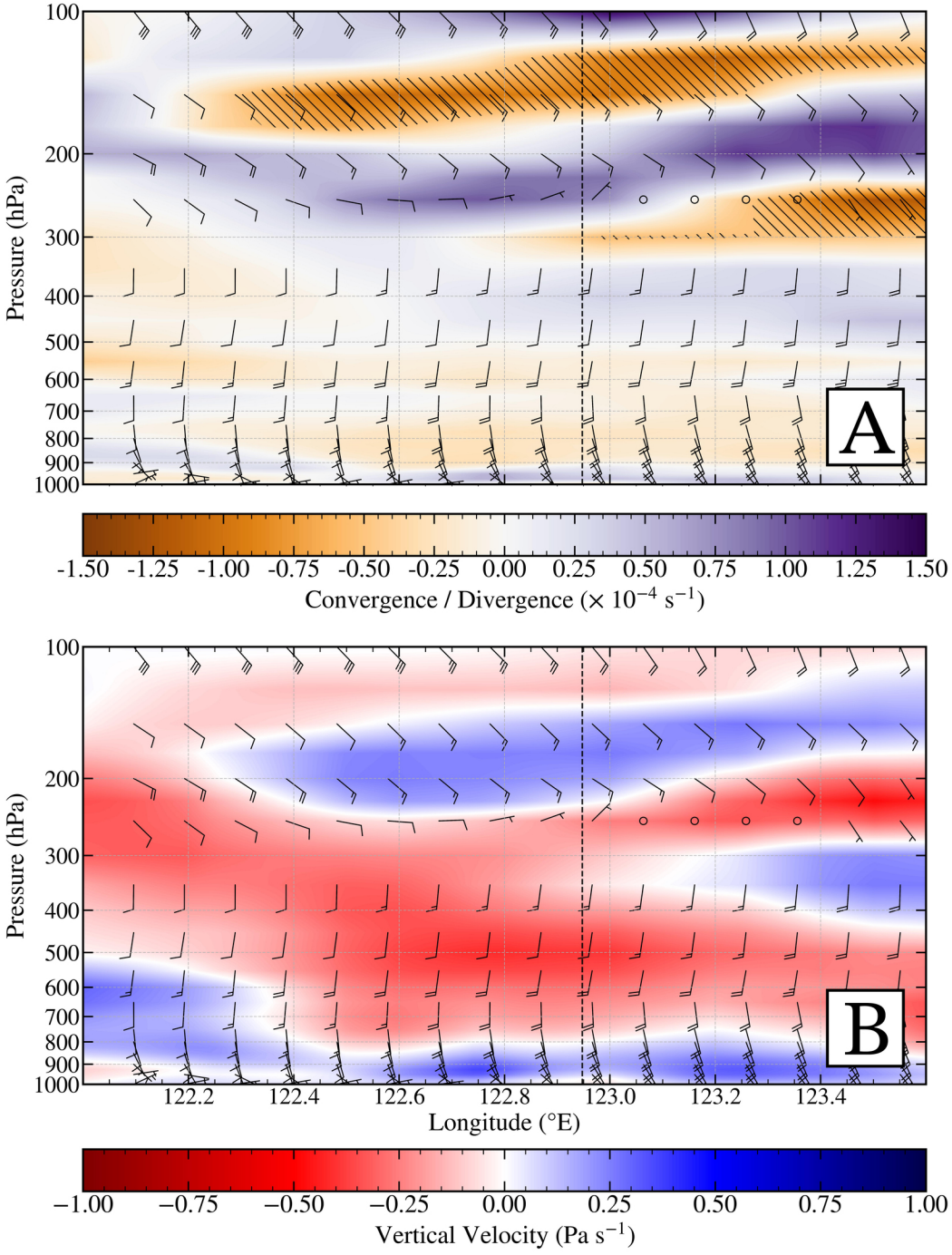


Figure 6. 22 UTC/06 LST ERA5 Vertical Cross Section of; (a) Convergence / Divergence (Pa s^{-1}) with hatched area of Convergence > –0.50 × 10^{-5} s^{-1} and (b) Vertical Velocity (Pa s^{-1}) with hatched area of Convergence > –0.50 Pa s^{-1}. Both cross sections are accompanied by tangential and normal components (kt).

indicative of ample atmospheric instability. This also coincides with sufficient near-surface vorticity (> 1.0×10^{-5} s^{-1}) supportive of tornado-producing supercells. The overlap of these conditions is commonly observed in the Great Plains' Tornado Alley during spring-season severe weather outbreaks. In such regimes, the low-level shear vector often exhibits pronounced clockwise curvature with height, forming a 'sickle/hook shaped' profile that is favorable

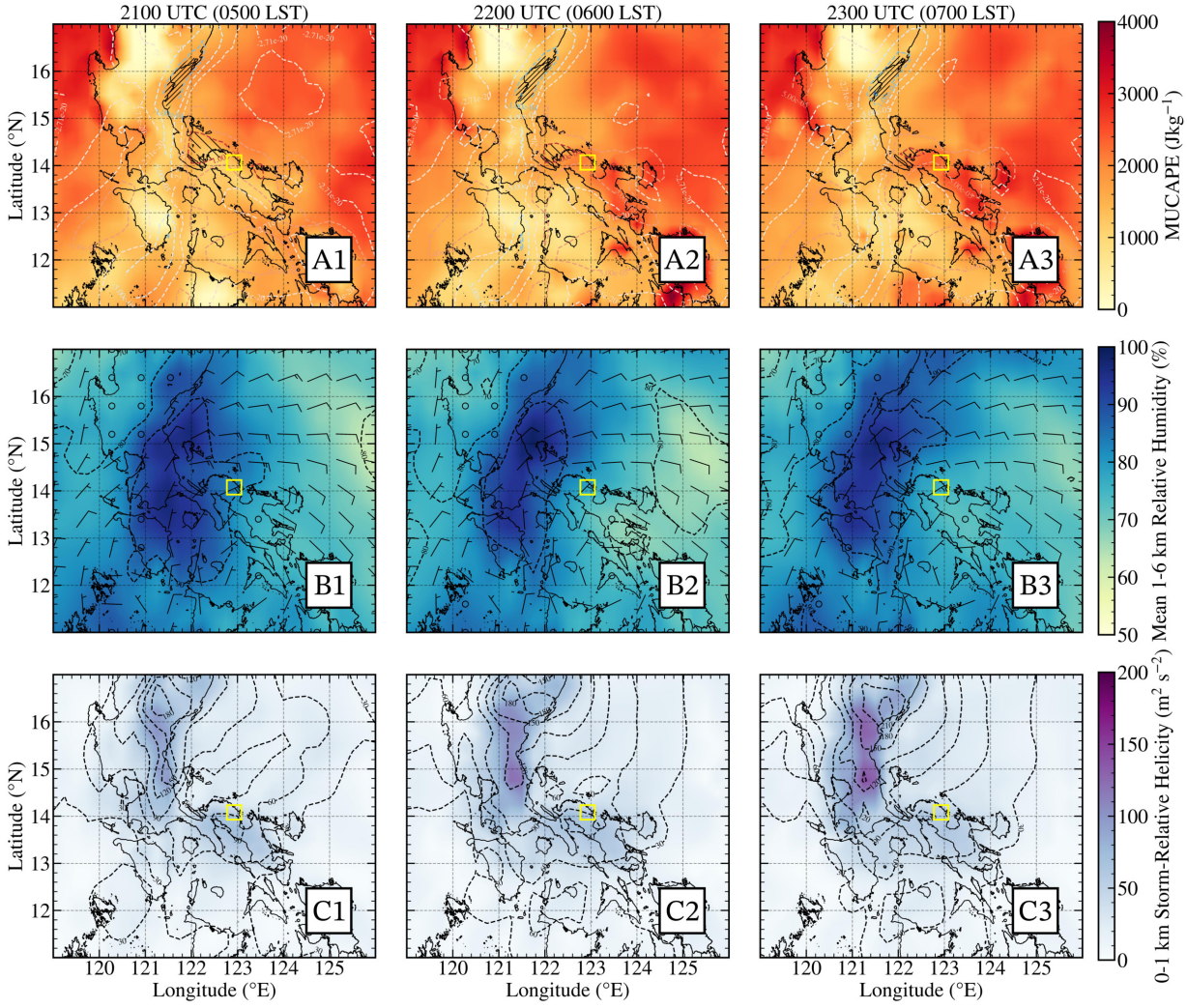


Figure 7. Convective and Kinematic environment of the Luzon landmass before (1; 21 UTC/05 LST), during (2; 22 UTC/06 LST), and after (3; 23 UTC/07 LST) the event. (a) MUCAPE (J kg^{-1}) and Surface Vorticity (gradient dashed; $\times$ 10^{-5} s^{-1}). (b) Average 1–6 km Relative Humidity (%), including Average 1–3 km Relative Humidity (black dashed; %), and 10-m Winds (kt). (c) 0–1 km and 0–3 km SRH (black dashed; m^2 s^{-2}). The case area is demarcated in yellow box.

for the development of tornadic supercells (Weisman and Klemp 1986; Thompson and Edwards 2000; Coffer et al. 2020; Nixon and Allen 2022). In Figures 7b1–b3, the low-level and mid-level RH fields show a moist environmental profile, particularly before the event, with RH$_{13}$ > 80% across the Daet, Camarines Norte region (highlighted in the yellow box). To the west of the storm initiation zone, RH above the cloud base exhibited RH$_{13}$ > 90%, which may have contributed to the maintenance of additional convective development. Peters et al. (2022b,a) emphasized that free-tropospheric moisture is fundamental to convection initiation, governing the likelihood of convective updraft formation. This moist environment was superimposed with modest 0-1 km and 0-3 km SRH exceeding 70–100 m^2 s^{-2} within both layers, as illustrated in Figures 7c1–c3. These conditions indicate that the combination of thermodynamic instability and kinematics was strongly enhanced by the approach of the inverted trough and the advection of moist air via the prevailing southeasterly-to-easterly flow. This in turn facilitated increased CAPE and provided sufficient buoyancy to sustain robust convective updraft, capable of ingesting vorticity for tornadogenesis (Púčik et al. 2015).

To further examine the evolving thermodynamic and kinematic environment, Figure 8 presents the derived model sounding and hodographs at 21, 22, and 23 UTC (05, 06, and 07 LST 13 September 2026) representing the before, during, and after the tornado event. The model soundings (Fig. 8a1–a3) exhibit a moist tropical profile

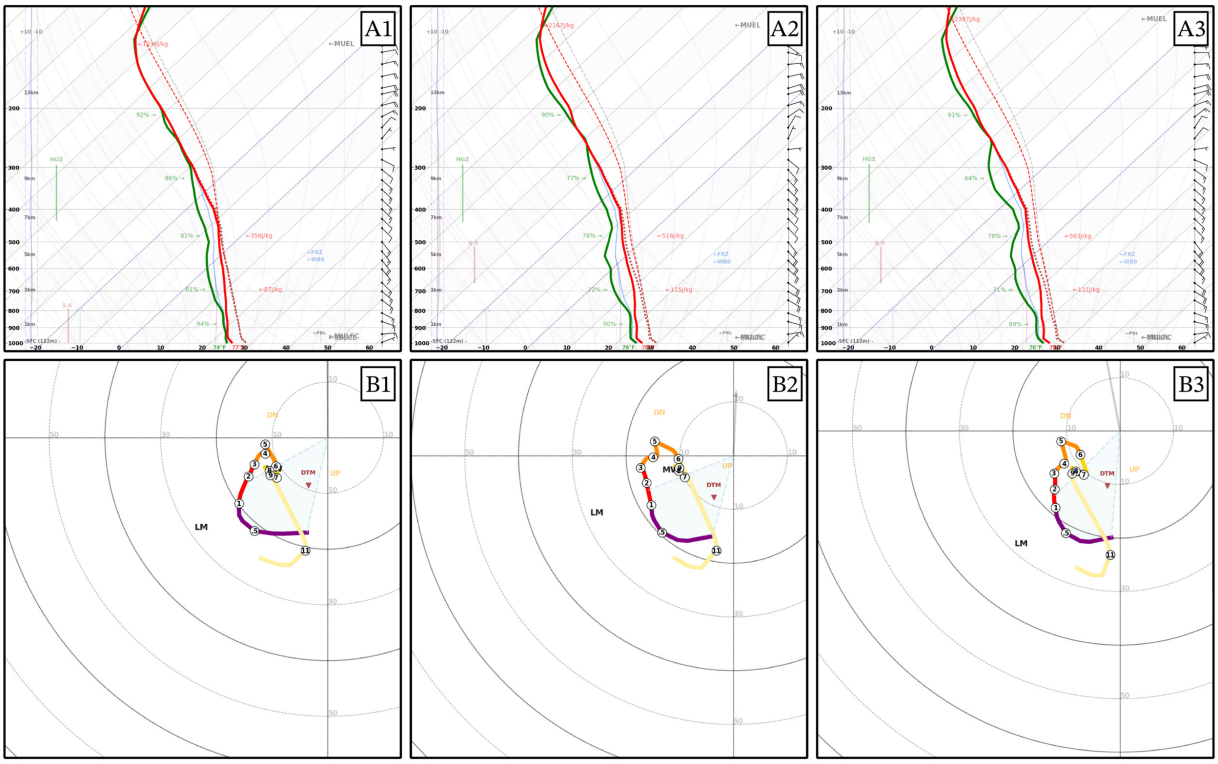


Figure 8. ERA5 Sounding Profile before (1; 21 UTC/05 LST), during (2; 22 UTC/06 LST), and after (3; 23 UTC/07 LST) the event. (a) Thermodynamic profile along the area of interest. Annotations to the thermodynamic profiles include the SBLCL, PBL, MULFC, FRZ, and MUEL. (b) Storm-relative Hodographs associated with the thermodynamic profile above. Annotations to the wind profiles include the individual Bunkers' Storm Motion, Deviant Tornado Motion, and Corfidi's MCS components.

characterized by a small *dewpoint depression*[7] from the near-surface to around 800-hPa, the absence of a significant inhibition layer (CIN $\sim$ 0 J kg^{-1}), and low LCLs ranging from 150–200 m AGL. Additionally, the profiles indicate a moist PBL with $RH_{13} > 80\%$, with mid-level lapse rates improved from 5.39 °C km^{-1} to almost 6 °C km^{-1} by the time of the tornado occurrence. The moisture quality between the lower and mid-tropospheric levels (represented by RH_{16}) only decreased subtly due to the start of surface heating, but this subtle decrease in mid-level moisture aided in the thermodynamic environment to be favorable for convective development. Before the event (21 UTC/05 LST), the profile is mostly defined by thin-skinny moist profile resulting in undiluted CAPE of 1336 J kg^{-1} with most of the instability layer confined above 400-hPa. Due to the nature of the thermodynamic profile, $CAPE_{03}$ were also minimal < 100 J kg^{-1} thereby initially limiting parcel buoyancy in the low-levels. However, at 22 UTC (06 LST), coinciding with the tornado occurrence, CAPE exceeds 2167 J kg^{-1} with low-level CAPE breaching > 100 J kg^{-1} threshold (115 J kg^{-1} to be exact) due to the subtle decrease of mid-level RH while steepening of MLLR. The abundance of low-level instability in the environment is important in the tornadogenesis process as it can lead to higher vertical velocities near the surface. Markowski and Richardson (2010) stated that once a tornado becomes established, tilting of the surface-layer horizontal vorticity by the extreme vertical velocity gradient associated with the updraft itself probably contributes to the near-ground vertical vorticity in a significant way. This substantial increase in instability, coupled with low LCLs, highlights a thermodynamic environment that strongly favored surface-based severe storms capable of producing tornadoes (Grünwald and Brooks 2011; Matsui et al. 2016).

One defining feature of the modeled hodographs associated with this event was their unusual orientation (Fig. 8b1–b3). The storm-relative hodograph exhibited a low-level clockwise rotation of the wind profile where winds originate from the east-southeast diverging from the classical configuration (south-southwesterly), indicating a unique shear environment. This wind profile produced a DLS vector that supported supercells with northeastward motion, with right-moving (RM) supercells veering further northward. Such hodograph shape is unusual and has not been documented elsewhere wherein easterly windflow manifested as hook-shape/curved hodographs

[7]Dewpoint depression means the difference between the temperature and dewpoint temperature. Lower $T - T_D$ spreads mean moist profile.

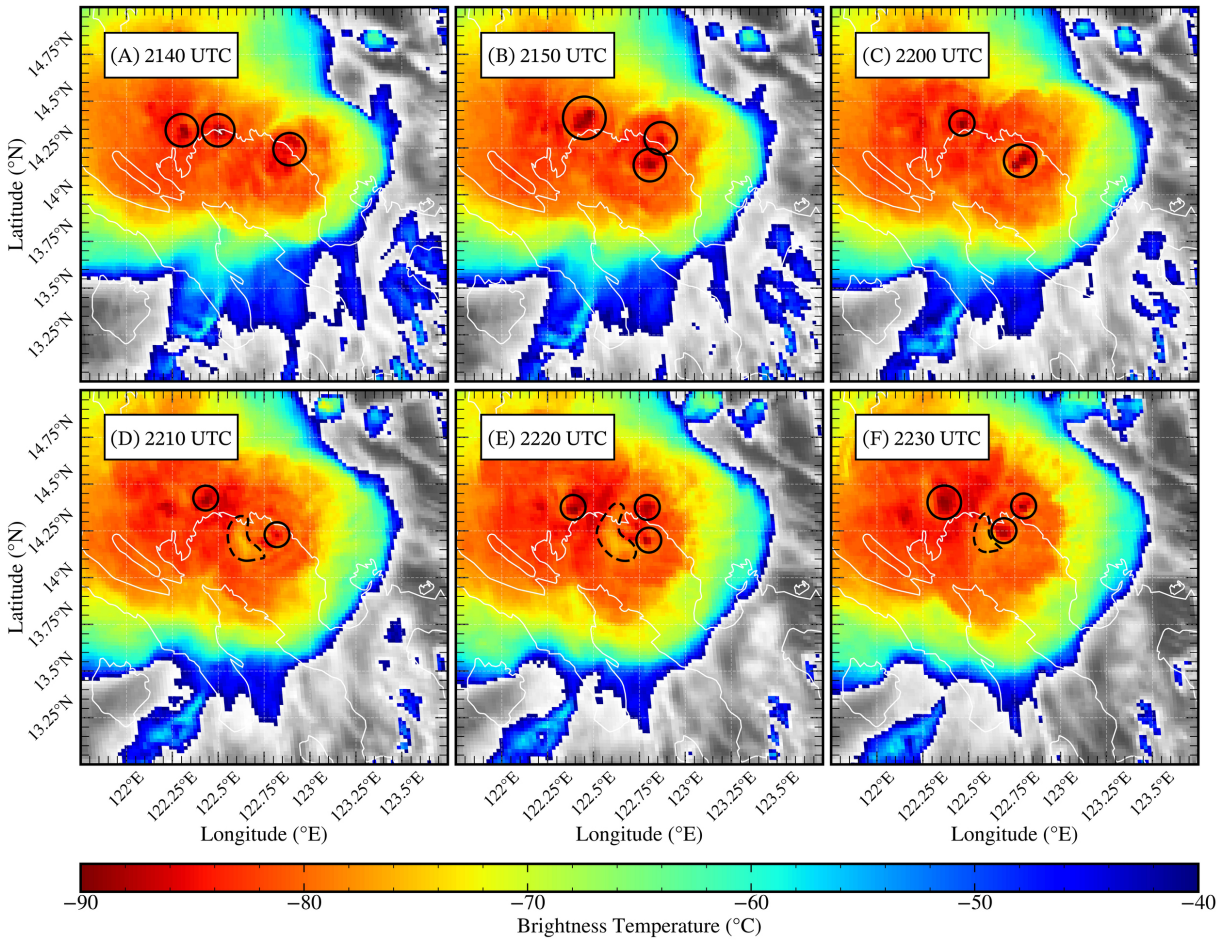


Figure 9. HIMAWARI-9 AHI 10.4 μm BT depicting MCS evolution dated 13 September 2025. Each scans are every 10 minutes, starting at 2140–2230 UTC (0540–0630 LST; a–f). Black circles are areas of identified OTs, while the dashed lines are the AACPs.

and eventually produced tornadoes. Unlike in the warm-season North American Monsoon regime (NAM; Adams and Comrie 1997; Blanchard 2011) where low-level south-westerlies accompanied by northeasterly winds aloft produces hodographs that can favor hook echo signatures in the northwestern quadrant of supercells, this east-southeasterly-driven hodograph favors hook echo located on the southern to southeastern side of the storm (i.e., lower-right flank of the storm). In this case, RM storm motions play at around 180° at speeds of 12–17 kt (6–9 m s^{-1}) with a vector-averaged mean motion of ~150° at 16 kt (8.23 m s^{-1}). Although the presence of hodograph curvature is evident, the LLS remains weak (between 6–7 m s^{-1}) as compared to tornadic supercells recorded in the Great Plains with median LLS at around 11 m s^{-1} (Nixon and Allen 2022). Regardless, this still affirms work by Coffer et al. (2020) that significant tornadoes tend to have sufficient concentrations of SRH in the low-levels (between half kilometer to 1 km). Modest V_{SR} remained between to ~17-19 kt which helped mitigate the negative impacts of entrainment dilution on supercell's updraft. A fractional entrainment of > 70% was computed throughout the sounding analysis, indicating that the storm's updraft retained a substantial portion of the undiluted CAPE. This suggests that more than half of the available convective energy was effectively converted into updraft kinetic energy (Romps and Kuang 2010; Peters et al. 2019).

Additional kinematic parameters derived from the model storm-relative hodographs further support a favorable tornadic environment. The ambient near-surface horizontal vorticity is sufficient (~0.009 s^{-1}), and is highly parallel to the storm-relative flow near the time of tornadogenesis at 22 UTC (06 LST), with $\widetilde{\omega_{s500}} > 90\%$. In the lowest 1 km layer, streamwise vorticity also remained modest in magnitude and was highly streamwise throughout the analysis period, with $\widetilde{\omega_{s01}} > 90\%$. High streamwiseness, particularly from the surface to the cloud base, are crucial for tornadogenesis as they allow environmental vorticity to be more readily ingested, tilted, and stretched into the vertical by the storm's updraft.

Parameter	Definition	Notes	21 UTC ERA5	22 UTC ERA5	23 UTC ERA5
CAPE	Convective Available Potential Energy	MU Parcel	1336 J kg^{-1}	2167 J kg^{-1}	2387 J kg^{-1}
$CAPE_{03}$	0–3 km CAPE	MU Parcel	87 J kg^{-1}	115 J kg^{-1}	131 J kg^{-1}
$CAPE_{06}$	0–6 km CAPE	MU Parcel	356 J kg^{-1}	516 J kg^{-1}	563 J kg^{-1}
ECAPE	Entraining CAPE	MU Parcel	1071 J kg^{-1}	1534 J kg^{-1}	1766 J kg^{-1}
CIN	Convective Inhibition	SB Parcel	0 J kg^{-1}	0 J kg^{-1}	0 J kg^{-1}
LCL	Lifted Condensation Level	SB Parcel	157 m	180 m	197 m
LFC	Level of Free Convection	MU Parcel	157 m	180 m	197 m
LR_{03}	0–3 km Lapse Rate	Low-level	5.52 °C km^{-1}	5.63 °C km^{-1}	5.74 °C km^{-1}
LR_{36}	3–6 km Lapse Rate	Mid-level	5.39 °C km^{-1}	5.84 °C km^{-1}	5.88 °C km^{-1}
RH_{13}	Mean 1–3 km Relative Humidity		0.90 / 90%	0.86 / 86%	0.84 / 84%
RH_{16}	Mean 1–6 km RH		0.83 / 83%	0.77 / 77%	0.76 / 76%
BWD_{01}	0–1 km Bulk Wind Difference	LLS	13.82 kt / 7.12 m s^{-1}	12.85 kt / 6.61 m s^{-1}	11.83 kt / 6.09 m s^{-1}
BWD_{03}	0–3 km BWD	MLS	15.46 kt / 7.95 m s^{-1}	18.52 kt / 9.53 m s^{-1}	16.10 kt / 8.28 m s^{-1}
BWD_{06}	0–6 km BWD	DLS	13.16 kt / 6.77 m s^{-1}	15.77 kt / 8.11 m s^{-1}	16.54 kt / 8.50 m s^{-1}
BWD_{13}	1–3 km BWD		7.58 kt / 3.90 m s^{-1}	7.22 kt / 3.71 m s^{-1}	6.45 kt / 3.32 m s^{-1}
BWD_{16}	1–6 km BWD		3.84 kt / 1.98 m s^{-1}	7.20 kt / 3.70 m s^{-1}	6.02 kt / 3.10 m s^{-1}
$B2K_{RM}$	Bunkers RM Storm Motion	Right Mover	15.23 kt / 7.84 m s^{-1}	12.10 kt / 6.22 m s^{-1}	17.47 kt / 8.99 m s^{-1}
V_{SR}	Mean 0–1 km Storm-relative Wind	$B2K_{RM}$	18.64 kt / 9.58 m s^{-1}	16.66 kt / 8.57 m s^{-1}	19.34 kt / 9.95 m s^{-1}
SRH_{500}	0–500 m Storm-relative Helicity	$B2K_{RM}$	43 m^2 s^{-2}	41 m^2 s^{-2}	48 m^2 s^{-2}
SRH_{01}	0–1 km SRH	$B2K_{RM}$	75 m^2 s^{-2}	68 m^2 s^{-2}	71 m^2 s^{-2}
SRH_{03}	0–3 km SRH	$B2K_{RM}$	96 m^2 s^{-2}	100 m^2 s^{-2}	93 m^2 s^{-2}
SRH_{13}	1–3 km SRH	$B2K_{RM}$	21 m^2 s^{-2}	32 m^2 s^{-2}	21 m^2 s^{-2}
ω_{s500}	0–500 m Streamwise Vorticity	$B2K_{RM}$	0.009 s^{-1}	0.009 s^{-1}	0.009 s^{-1}
$\widetilde{\omega_{s500}}$	0–500 m Streamwiseness	$B2K_{RM}$	0.9184 / 91.84%	0.9035 / 90.35%	0.9672 / 96.72%
ω_{s01}	0–1 km Streamwise Vorticity	$B2K_{RM}$	0.008 s^{-1}	0.008 s^{-1}	0.007 s^{-1}
$\widetilde{\omega_{s01}}$	0–1 km Streamwiseness	$B2K_{RM}$	0.9261 / 92.61%	0.9290 / 92.90%	0.9089 / 90.89%
ζ_{LLM}	0–1 km Low-level Vertical Vorticity	MU Parcel	0.016 s^{-1}	0.020 s^{-1}	0.016 s^{-1}
DTM	Deviant Tornado Motion	$B2K_{RM}$	7.11 kt / 3.66 m s^{-1}	5.39 kt / 2.77 m s^{-1}	8.24 kt / 4.24 m s^{-1}
$W_{MAX}SHEAR$	Undiluted Updraft Velocity × BWD_{06}	MU Parcel	494.91 m^2 s^{-2}	755.06 m^2 s^{-2}	830.58 m^2 s^{-2}
SCP	Supercell Composite Parameter		1.67	2.64	2.54
STP	Significant Tornado Parameter		0.37	0.60	0.56

Table 2. ERA5 Sounding-derived measurements associated with the tornado outbreak

Although the model soundings did not resolve enhanced low-level shear (LLS < 10 m s^{-1}), given its coarse resolution, topographically induced modifications were likely present. Specifically, terrain-driven processes where low-level southeasterly flow impinged on the surrounding high terrain and was subsequently deflected/channeled along the foothills and coastal plain, favoring a quasi-stationary low-level confluence boundary that concentrates horizontal shear and cyclonic vertical vorticity i.e., a terrain-anchored convergence–vorticity zone, analogous in mechanism to the Denver Convergence Vorticity Zone (DCVZ)[8], can precondition the environment for convective initiation and locally enhanced rotation via convergence-forced ascent and vorticity stretching (Szoke 1991; Wilczak et al. 1992; Kirshbaum et al. 2018; Trier et al. 2019). Such terrain influences are consistent with the numerical simulation results of Bosart et al. (2006) for the Great Barrington, Massachusetts F3 tornado, who showed that tornadogenesis becomes more likely when local terrain-driven perturbations to the low-level flow enhance near-storm convergence and vertical vorticity. When this enhancement occurs in an environment characterized by ample streamwise vorticity in the lowest half to a kilometer, collocated with ample $CAPE_{03}$ and vertical vorticity in the low-level mesocyclone (ζ_{LLM}) exceeding 0.01–0.02 s^{-1} throughout the analysis period, convective-scale stretching and tilting processes can proceed efficiently, increasing the likelihood that a supercell produces a tornado (Coffer et al. 2023).

The composite parameter $W_{MAX}SHEAR$, which combines instability i.e., CAPE and DLS, exceeded 755 m^2 s^{-2} near the time of the tornadic event, representing a significant increase from the initial sounding of ≤ 500 m^2 s^{-2}. This magnitude falls well within the climatological range associated with environments favorable for severe convection and tornadogenesis (Taszarek et al. 2020b). In addition, the Supercell Composite Parameter (SCP) reached 2.6, while the Significant Tornado Parameter (STP) was 0.6. Although modest, these values fall within the outer bounds of the baseline climatology for significant tornadic

[8]DCVZ is a well-documented mesoscale phenomena of enhanced low-level convergence and cyclonic vorticity that forms east of Denver as moist southeasterly upslope flow interacts with the Palmer Divide and terrain-modified flow from the Rocky Mountain foothills, focusing convective initiation.

supercells reported by Thompson et al. (2003), indicating an environment supportive of supercell thunderstorms with tornadic potential. Together, these parameters suggest that the background environment was favorable for discrete tornadic supercells. Moreover, additional mesoscale influences, particularly terrain-induced modifications (as discussed above), likely enhanced the ambient kinematics and buoyant instability available for storm development. However, the persistence, spatial extent, and tornadic nature of these storms may also be attributed to internal storm-scale dynamics, which will be addressed in the following subsection. A summary of key thermodynamic and kinematic indices derived from the ERA5 model sounding is provided in Table 2 for comparison and reference.

d. Storm Development and Life Cycle

1) Supercells' Characteristics

The temporal evolution of the convective storm is illustrated in Figure 9 using 10-minute interval scans from HIMAWARI-9 between 2140–2230 UTC (0540–0630 LST). While satellite data prior to 0410 UTC and beyond 0500 UTC are not visualized, the relevant information outside this period is discussed to provide a descriptive context of the storm's life cycle.

At 2100 UTC (05 LST), the Southern Luzon Regional Services Division of DOST-PAGASA (otherwise known as PAGASA-SLPRSD), issued its Regional Weather Forecast[9] within its domain area and asserted that cloudy skies and scattered rainshowers caused by thunderstorms is possible to affect the Camarines Norte accompanied by light to moderate surface winds generally from the east. The aforementioned office also issued a Heavy Rainfall Warning No. 3[10] focused along Camarines Norte due to the low pressure system affecting the area of interest, which can also cause flooding and landslides in higher terrain.

Satellite IR imagery taken by HIMAWARI-9 shows the severe convective storm already persisting and affecting the coastal areas of Southern Luzon, primarily along Camarines Norte. The convection is depicted with anvil plume exceeding –75 – –80 °C or colder, presence of above anvil cirrus plumes (AACPs), and multiple OTs at –90 °C all due to intense updrafts penetrating the tropopause. These satellite features are tell-tale signs of severe weather in the region capable of producing significant wind, hail, and/or tornadoes (Schmit et al. 2013; Bedka et al. 2015, 2018). The severe storm also produced intense lightning activity ahead of the tornado event, as seen in Figure 10, with the vast majority of its CG output delivered in positive polarity (73%), as compared to negative polarity (27%). However, –CG lightning exhibited stronger peak currents, even for –CGs that are <–10 kA, than positive CG lightning with maximum –CG rate exceeding 133 flashes min^{-1} in one point of the storm lifecycle. A summary of the severe thunderstorm's lightning property is in Table 3. Upon further satellite inspection, the calculated r from the B13 is at 113 km. Given its large spatial coverage satisfying the storm scale thresholds (e.g., > 100 km; Carvalho and Jones 2001) and the presence of multiple OTs, this can be classified as a tropical MCS with embedded supercells within the cloud head. Embedded supercells within the greater storm complex have been documented many times in past studies, such as in CONUS, they have attributed 13.8% to 21% of all tornadoes to QLCS convective modes (Ashley et al. 2019; Smith et al. 2012).

Storm cell duration	~2:10 hr
−CG Flashes	1604 flashes
−CG Flashes with peak currents < −10 kA	413 flashes
+CG Flashes	4328 flashes
+CG Flashes with peak currents > 10 kA	271 flashes
Average peak current for −CG (kA) (median)	−7910.23 kA (−3841.51 kA)
Average peak current for −CG (< −10 kA) (median)	−20319.87 kA (−16927.05 kA)
Average peak current for +CG (kA) (median)	4290.61 kA (2787.04 kA)
Average peak current for +CG (> 10 kA) (median)	19128.54 kA (14185.73 kA)
Maximum Total Flash Rate (min^{-1})	173 flashes min^{-1}
Maximum −CG Rate (min^{-1})	133 flashes min^{-1}
Maximum +CG Rate (min^{-1})	59 flashes min^{-1}

Table 3. Overall lightning characteristics of the storm cell.

To complement the satellite-based analysis, radar scans from the S-DAT were analyzed. Both Figures 11 and 12 represent the evolution of the tornadic supercells from 2200–2230 UTC (0600–0630 LST) at 10-minute intervals. Figure 11 is composed of both Z_H and V_R scans, while Figure 12 introduces the polarimetric variables such as Z_{DR} and ρ_{HV} using the 4th radar elevation angle (3.4°; roughly 300–500 m above radar level within 10 km coverage). Both figures are accompanied by a 'zoomed in' version from subfigures no. 5–8 e.g., Fig. 11a5–a8, therefore, will be used in this discussion, which is highlighted subfigures no. 1–4 as dashed blue lines.

Reflectivity scans (Fig. 11a5–a8) depicts a complex of SCS in the area. By the 2210 and 2220 UTC (0610 and 0620 LST) volume scans, three distinct supercells had become apparent, each outlined in black. These are labelled as 'TS1' (Tornadic Supercell No. 1), identified as the Magang tornado-producing storm; 'TS2', associated with the Cahabaan tornado in Talisay; and 'TS3', linked to the Napilihan tornado in Vinzons which likely to be brief. Unfortunately, the Lag-On tornado identified earlier was not resolved by the radar given its close proximity to the radar site's cone of silence. Both TS1 and TS2 exhibited maximum Z_H > 60 dBZ, coinciding with the satellite-identified OTs (BT < –80 °C), indicative of persistent and vigorous updraft activity. In particular, TS1 also exhibited an intense TDS (also coincident with the tornado vortex signature or TVS - radial velocity couplet; Ryzhkov et al. 2005; Brown and Wood 2012) of 65 dBZ. Additionally, a small-thin convective element (dashed outline) was lo-

[9] RWF: https://www.facebook.com/share/p/18jTVcruRd/

[10] HRW No. 3: https://www.facebook.com/share/p/1JUc5TR4yo/

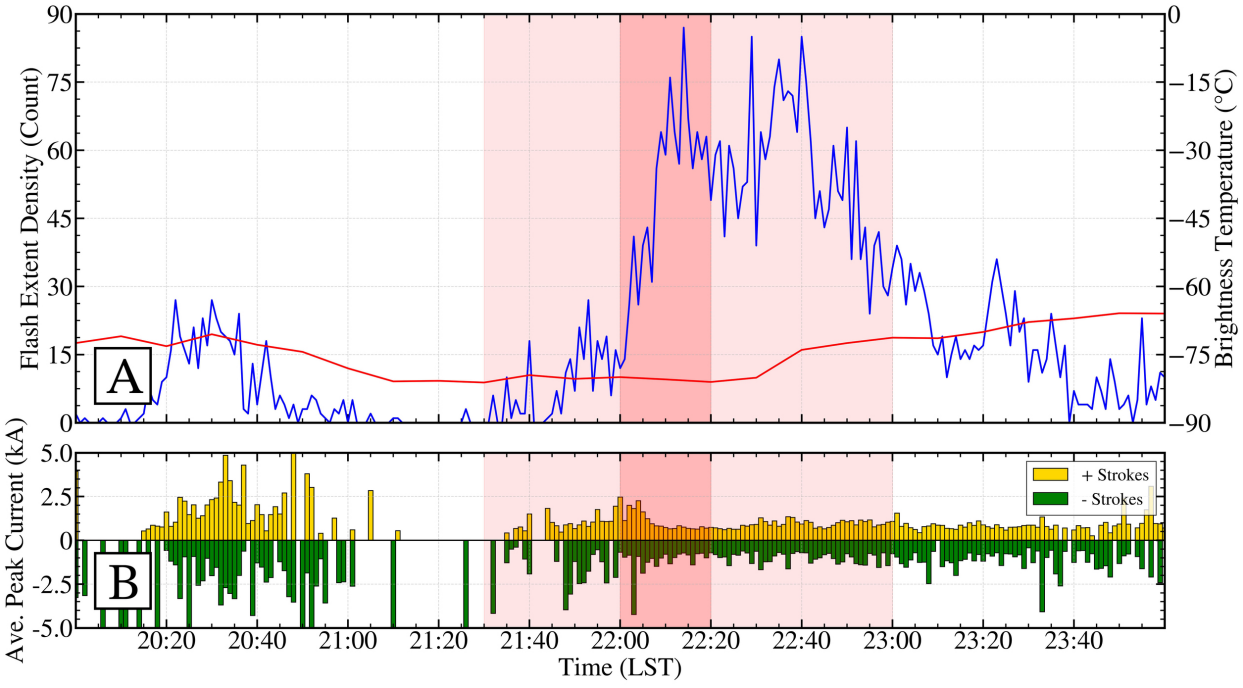


Figure 10. Time series of (a) Minimum 10.3 μm brightness temperature of the convective storm (red; °C), maximum flash extent density per minute (blue; counts or flashes min^{-1}). (b) Average Peak Current (kA) per minute of recorded Positive (yellow) and Negative Strokes (green) within the supercell. Highlighted in the time series are the estimated severe thunderstorm occurrence (light red) and tornadic event (dark red).

cated along the rear flank of the parent TS1 storm. The Z_H structure is unusual for a supercell morphology, but seems to have its own hook echo signature and a rear flank downdraft gust front (RFDGF) at the tip of this radar signature. We labelled this as a potential landspout vortex or may have been a representation of non-supercellular landspout processes. At the rear flank of TS1, TS2 also convected due to the present volatile environment. Eventually, at 2220 UTC (0620 LST), both tornadic supercells are still present and in-close proximity to one another with TS1 was still accompanied by a strong TDS. The storm-relative configuration aligns with the results of Nixon et al. (2024), which suggests that in supercell pairs, both the head and rightmost supercells, have the higher chance to become tornadic by achieving inflow-outflow balance thereby decelerating pre-tornadic vertical advection; a known precursor to tornadogenesis under weak storm relative inflow (Dowell and Bluestein 2002). In fact, TS2 eventually became tornadic as the presence of a weak-echo hole (WEH; Fujita 1981; Wakimoto et al. 1996; Wurman et al. 1996; Wakimoto et al. 2011; Wurman and Gill 2000; Bluestein et al. 2007b; Wurman and Kosiba 2013; Wakimoto et al. 2015, 2025, and references therein) with lowered Z_H signal of 46 dBZ and inflow channel coinciding with the development of the streamwise vorticity current (SVC; Klemp and Rotunno 1983; Orf et al. 2017; Schueth et al. 2021, and references therein) was depicted. The formation of WEH within the tornado core is likely caused by the centrifuging of hydrometeors and debris (Dowell et al. 2005).

A key feature observed in the radial velocity scans was the emergence of several velocity couplets in form of TVSs between 2210 and 2220 UTC (0610–0620 LST), marked in Figure 11b2–b3 and Figure 11b6–b7 (yellow circles). These couplets are indicative of a mesocyclonic circulation consistent with tornadic potential. Initially, there's an increase in inbound velocities from 2200 UTC (0600 LST) to tornado initiations accompanied by the convergence couplets at 2210 UTC for both supercells. With the MDA and its thresholds applied, TS1 had initial V_{rot} of 12.44 m s^{-1} and radar-derived vorticity of 0.049 s^{-1}, while TS2's V_{rot} is at ~7 m s^{-1} and radar-derived vorticity of 0.028 s^{-1}. By 2220 UTC, V_{rot} measurement is still ~10 m s^{-1} with vorticity of 0.039 s^{-1} for TS1, while TS2 further strengthened with V_{rot} values at 9.5 m s^{-1} and ζ_{rad} of 0.037 s^{-1}. The maintenance and rapid intensification/growth from this MDA strongly indicate the development of potential mesocyclones capable of producing tornadoes to each supercells. Notably, the ζ_{rad} aligns with the sounding-derived ζ_{LLM} ~ 0.015–0.020 s^{-1} indicating that severe thunderstorms can attain low-level rotation, thereby consummating a tornado and lending additional confidence to the interpretation. The location of TS1 and TS2's velocity couplets coincide spatially and temporally with the development of a hook echo signature and TDS, a

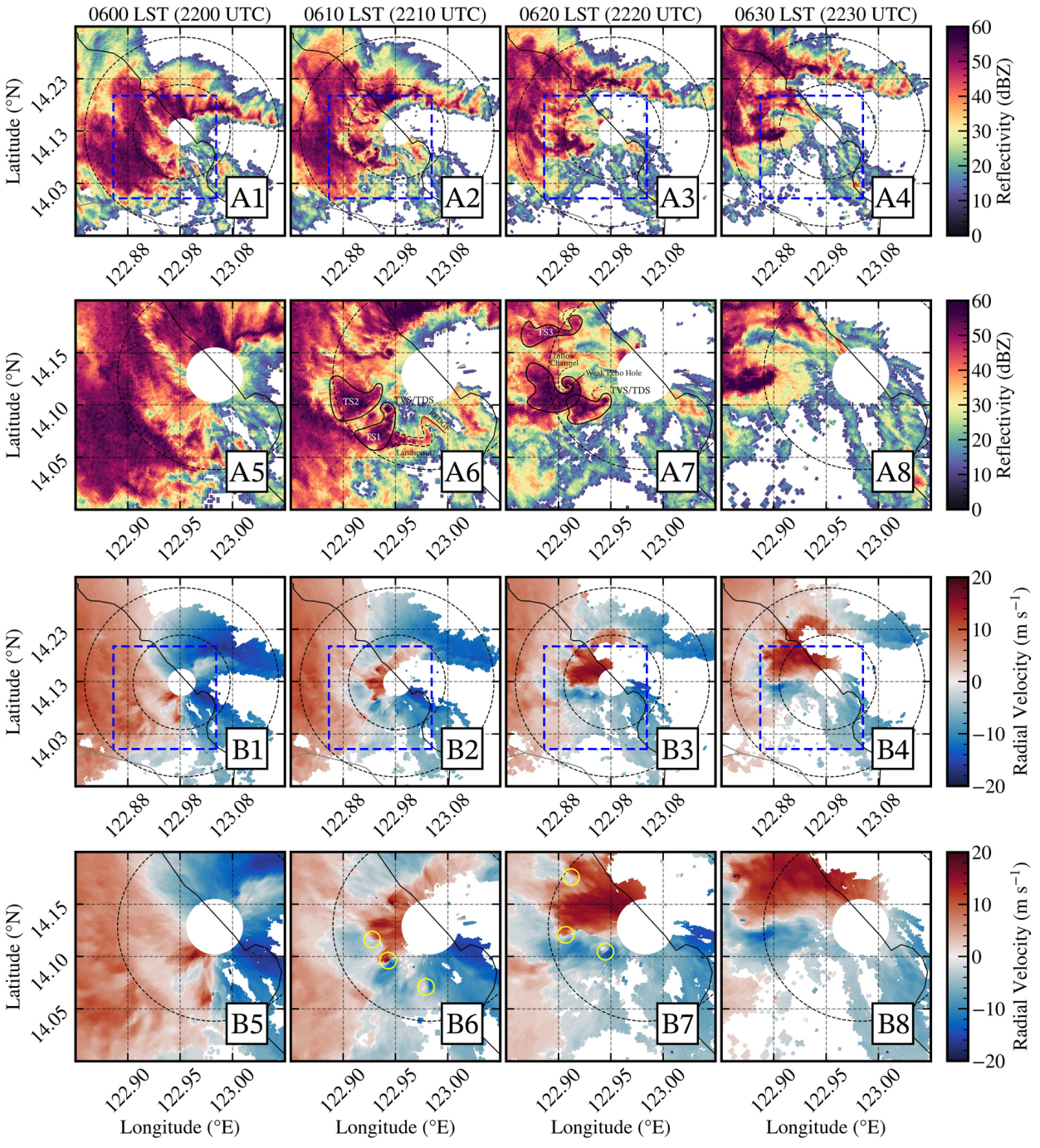


Figure 11. S-DAT 3rd elevation scans (3.4°) of the tornadic supercell for every 10 minutes. Radar variables include (a) Reflectivity (dBZ) and (b) Radial Velocity (m s^{-1}). Time stamps start from 2200–2230 UTC (0600–0630 LST). Both a5–a8 and b5–b8 sub-figures are 'zoomed in' radar scans to their respective time and radar products (as in dashed blue box). Annotations in the reflectivity field are included e.g., Tornadic Supercell (TS), Tornado Vortex Signature (TVS), while the yellow circles are the inherent velocity couplets.

classic radar feature associated with tornadic supercell. In particular, the presence of the velocity couplet and TDS for TS1 corresponds with visual and photographic evidence of the damage extent previously presented (Fig. 3), confirming the occurrence of the Magang tornado event.

Dual-polarimetric parameters were also evaluated in the presence of these embedded supercell storms. Figure 11

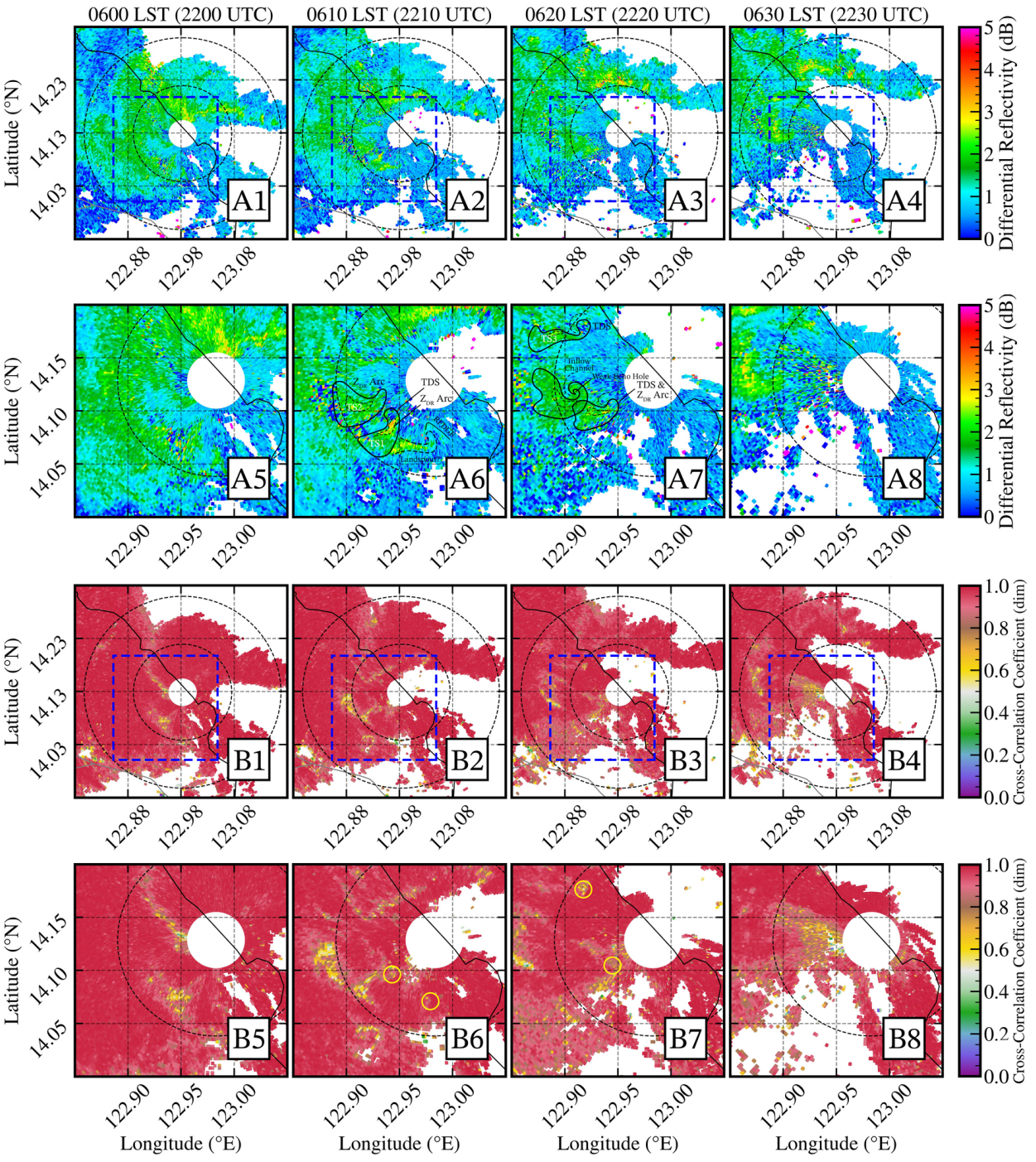


Figure 12. Similar to Figure 11 but (a) Differential Reflectivity (dB) and (b) Cross-Correlation Ratio (dimensionless). Time stamps start from 2200–2230 UTC (0600–0630 LST). Both a5–a8 and b5–b8 sub-figures are 'zoomed in' radar scans to their respective time and radar products (as in dashed blue box). Annotations in the differential reflectivity field are included.

showcases Z_{DR} (11a1–a8) and ρ_{HV} (11b1–b8) signatures of the storms' of interest, with subfigures no. 5–8 being the zoomed in version (similar to Figure 10). Starting with the parent storms, for TS1, the Z_{DR} field displayed values at around 2–3 dB along the forward-flank co-located with high reflectivities. Meanwhile, TS2's Z_{DR} field also showed values between 1.75–2.5 dB also collocated with high reflectivities in the FFD all the way to the hook echo.

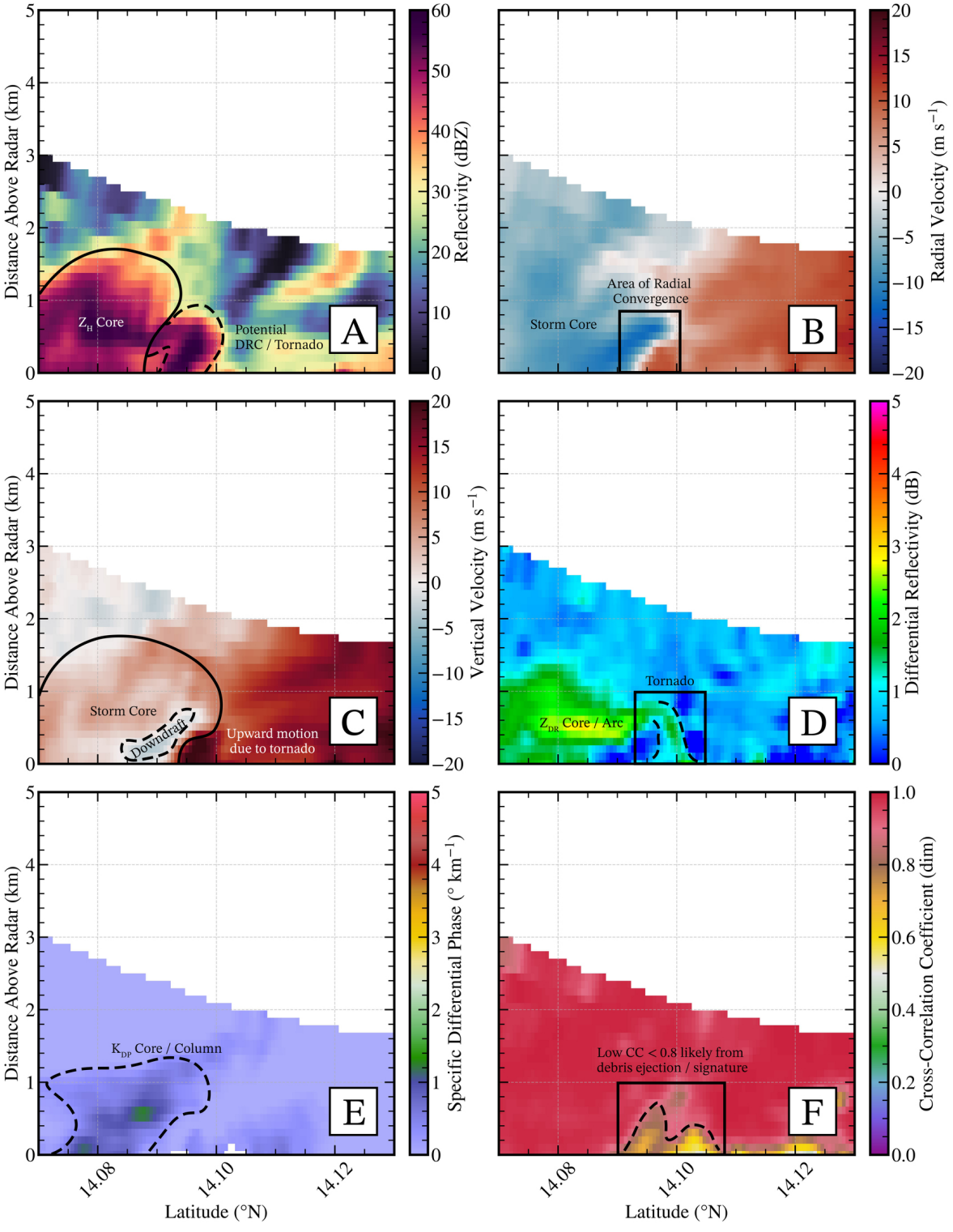


Figure 13. Vertical cross section of TS1 at 0610 LST (2210 UTC). (a) Reflectivity (dBZ), (b) Radial Velocity (m s^{-1}), (c) Vertical Velocity (m s^{-1}), (d) Differential Reflectivity (dB), (e) Specific Differential Phase (°km^{-1}), and (f) Cross-Correlation Ratio (dimensionless). Annotations are included in each sub-panel.

Furthermore, at 2210 UTC, an increased signal of Z_{DR} with high Z_H was located at the intersection of the FFD and the inflow notch of the low-level circulation. This feature is known as the Z_{DR} arc (Kumjian and Ryzhkov 2008). The Z_{DR} arc marked the zone of maximum gradient in echo intensity along the FFD region where measurements reached 3–4 dB for TS1, while ~2.25–2.8 dB for TS2, with varying unique placement of the Z_{DR} arc signatures to each storm of interest. For TS1, the polarimetric feature extends rearward very close to the TDS, while the Z_{DR} arc of TS2 is located mainly in the FFD extending towards the developing hook echo. Recent studies on tornadic supercells have demonstrated that additional polarimetric signatures can provide novel insights into the storm-scale processes required for tornadogenesis and maintenance (Kumjian and Ryzhkov 2009; French et al. 2015; Homeyer et al. 2020; Broeke 2020; Clark 2024). Thus, Z_{DR} arc features of the tornadic supercells could be an indication of enhanced SRH, and more importantly an indicator of storm severity since the ERA5 model sounding cannot capture completely the storm-scale evolution of SRH (Max SRH_{03} = 100 m^2 s^{-2} at the onset of tornado), but still gives a depiction of the environment conducive to severe weather. Such as that the Z_{DR} arc tends to extend back into the inflow notch of supercells (as seen in TS1 and TS2) leading up to the strengthening of the low-level mesocyclone and potential tornadogenesis. Furthermore, TS2 also exhibited an increase in the areal extent of the Z_{DR} field which is indicative of an increase in the low-level Z_H by 10–15 minutes (e.g., Picca et al. 2010).

Other storm traits were also evident at the time of tornado events. In particular, TS1 exhibited very low ρ_{HV} values (0.362 < 0.80)[11] and low Z_{DR} of –1.7 dB coinciding with the TDS and radial velocity couplet from earlier discussion. However, for TS2 especially during the time when the WEH was present, it is unclear why the 'ρ_{HV} depression' was not completely apparent in the 4th elevation scan (~490 m Above Radar Level/ARL), but in the 1st tilt (~100 mARL), it registered a ρ_{HV} = 0.736 and Z_{DR} = –2.5 dB, then transitioning to higher ρ_{HV} and positive ~ in the successive elevations. It can be attributed to precipitation entrainment such as observed by Bluestein et al. (2007a) likely hinting to a high-precipitation supercell and/or slightly elevated ρ_{HV} values within the minimum echo eye due to storm interaction (Schwarz and Burgess 2011)(. Despite the differences between the ρ_{HV} characteristics, it is clear that both tornadic supercells possessed near-ground debris signatures and satisfies the criterion for tornado detection as stipulated in Ryzhkov et al. (2005). Furthermore, a region of reduced ρ_{HV} (between 0.8 and 0.9), slightly positive Z_{DR}, and Z_H > 50 dBZ was also depicted and can be due to the presence of wet hail, or rain mixed with hail, within the forward flank core of the supercell thunderstorms. Such characteristics were also observed in a recent study by Clark (2024) on the Jersey tornadic supercell on midnight of 1–2 November 2023 where reduced ρ_{HV} in the TDS was observed coinciding with the reduced Z_{DR} (near-zero or even negative) and high Z_H.

[11] A ρ_{HV} threshold 0.80 delineates between hydrometeor vs non-hydrometeor species. Also known as ρ_{HV} debris signature, low ρ_{HV} can indicate non-meteorological scatterers such as natural ground cover (trees, grass, etc.), biological scatterers (insects, birds, and bats), and military chaff (Ryzhkov et al. 2005).

2) Vertical Cross Section of TS1 (Magang Tornado)

The vertical structure of the tornadic storm that produced the Magang Tornado was further examined using radar vertical cross-section analysis from the S-DAT radar. As illustrated in Figure 13, it provides details of the severe storm's vertical structure, oriented perpendicular to the storm structure (from the FFD to the TDS). A Z_H maxima of 64 dBZ (solid line, Fig. 13a) extending close to 2 km delineating the small core. Shown in dashed lines, there is also a signature of a Descending Reflectivity Core (DRC) within the rear-flank composed by heightened Z_H values (> 60 dBZ) connected within TS1's Z_H core. First observed by Rasmussen et al. (2006), DRCs are often found as a precursor of tornadogenesis and can form as a manifestation brought by the intensification of the low-level rotation (Byko et al. 2009).

Cross-sections of the V_R field (Fig. 13b) further substantiate the presence of a mesocyclonic circulation. A distinct velocity couplet structure, marked by juxtaposed inbound and outbound velocities, becomes particularly evident within the timing of the tornadogenesis. This feature is a classical indicator of low-level rotation and suggests the presence of a cyclonic vortex. This pair of opposite V_R was located near the surface and coincided with the DRC identified, affirming the intensification of the near-surface vortex. Along with updraft vertical velocities exceeding > 3–5 m s^{-1} indicative on-going convection (Fig. 13c), there is also a noticeable strip of negative vertical velocity anomalies near the surface which can be a signal of an axial downdraft (dashed lines; < –3 m s^{-1}) near the couplet. It has been observed that these downdrafts tend to develop in supercell thunderstorms (Klemp and Rotunno 1983) and as it intensifies near the rotation axis, it allows hydrometeors to descend toward the ground.

Shown in Fig. 13d, dual-polarimetric analysis of the TS1 reveals a Z_{DR} core (~2 dB), with the highest signal of the Z_{DR} arc (> 3 dB) also depicted within the sectional slice. This Z_{DR} signature can be identified as a Z_{DR} column where high values of Z_{DR} indicate the presence of large, oblate hydrometeors, presumably either large raindrops or water-coated hailstones. Warm-rain collision and coalescence processes are the possible origin of these hydrometeors (e.g., Caylor and Illingworth 1987; Tuttle et al. 1989; Meischner et al. 1991) or from back-sheared anvil

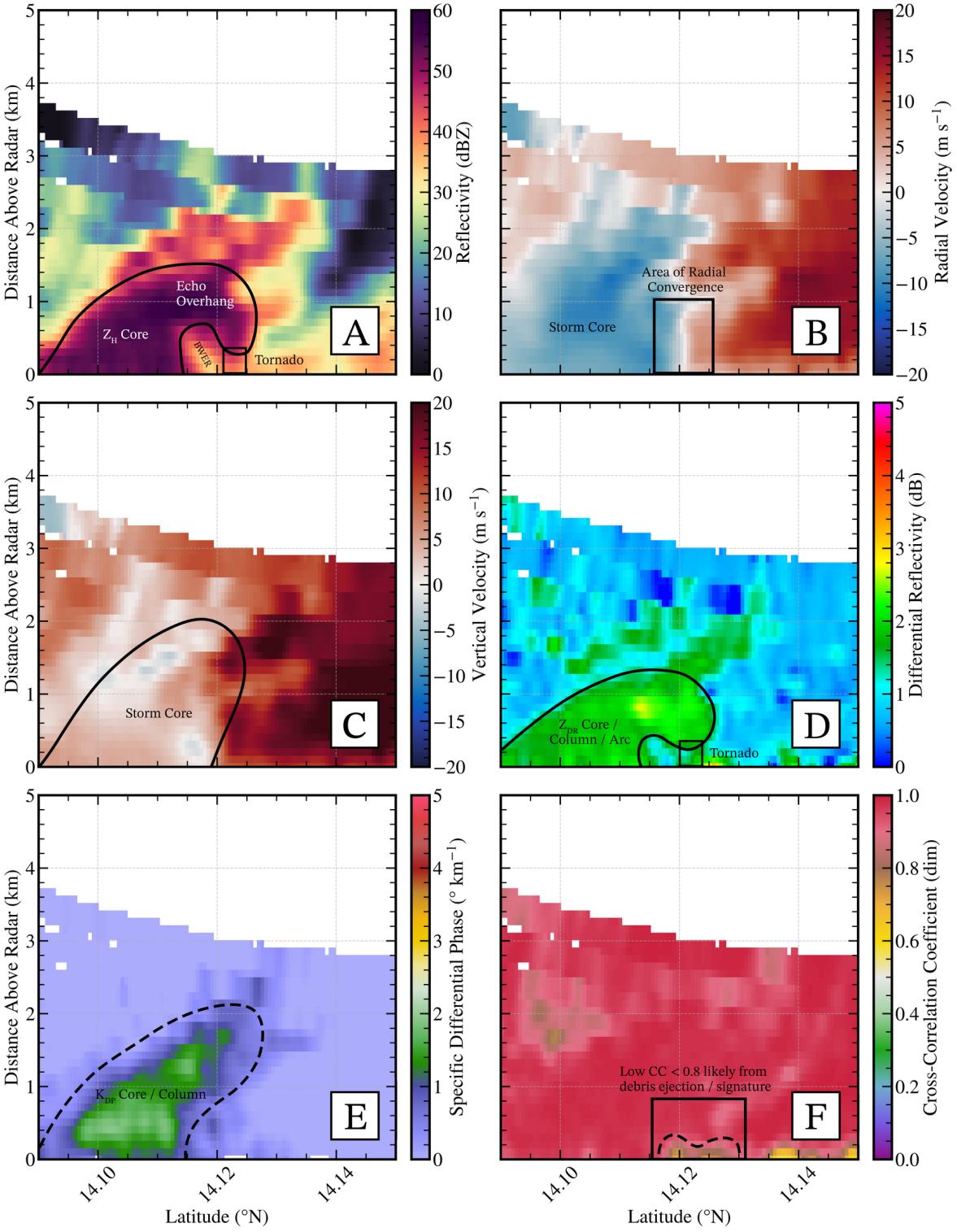


Figure 14. Similar to Figure 13 but for TS2 at 0620 LST (2220 UTC). (a) Reflectivity (dBZ), (b) Radial Velocity (m s^{-1}), (c) Vertical Velocity (m s^{-1}), (d) Differential Reflectivity (dB), (e) Specific Differential Phase (°km^{-1}), and (f) Cross-Correlation Ratio (dimensionless). Annotations are included in each sub-panel.

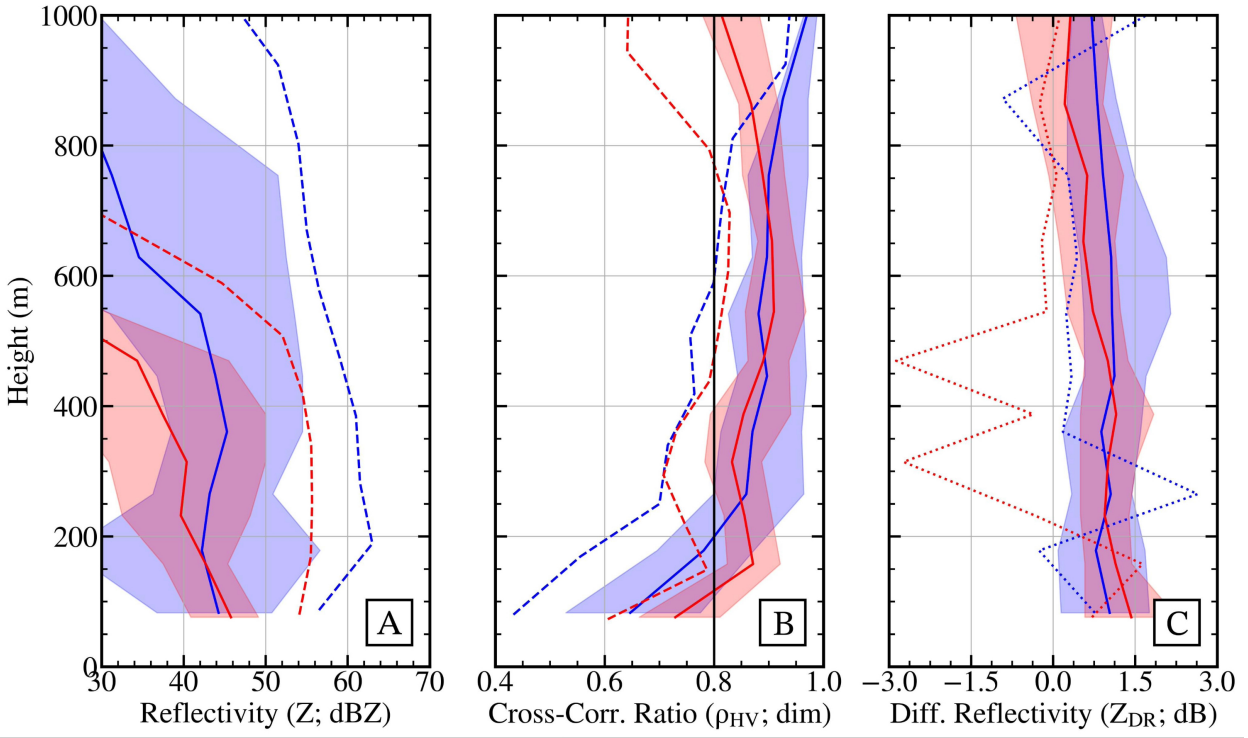


Figure 15. Angle-average vertical profiles of polarimetric variables in the TDS/TVS of TS1 (Magang Event) between 0610 LST (2210 UTC; Blue) and 0620 LST (2220 UTC; Red). (a) Reflectivity (dBZ), (b) Cross-Correlation Ratio (dimensionless), (c) Differential Reflectivity (dB). For panels (a) and (b), the solid line corresponds to the mean profile with 25th and 75th percentile contours, while the dashed lines are the 90th percentile (for Z_H) and 10th percentile (for ρ_{HV}). Meanwhile, for panel (c), the dotted lines represent the skewness of the Differential Reflectivity profile.

that are caught in low-level inflow and ingested back into the updraft (e.g., Conway and Zrnić 1993; Hubbert et al. 1998; Loney et al. 2002). In addition, Snyder et al. (2017) found that the DSD profile of supercells' Z_{DR} columns are associated with larger median rain drop sizes. The location of TS1's Z_{DR} core/column is found on the inflow side of the storm within the updraft and is consistent in observational studies conducted by Kumjian and Ryzhkov (2008). Also, due to the modest vertical velocity retrievals (as shown in Fig. 13c), a hydrometeor fallout is also recorded viewed as slightly enhanced Z_{DR} values of ~1.5 dB in the FFD < 500 mARL. This is consistent with Conway and Zrnić (1993) and Loney et al. (2002), who found the maximum values of Z_{DR} to be coincident with weaker vertical velocities in the convective updraft.

Aside from multiple Z_{DR} structures revealed, there is also the presence of a K_{DP} column with a noticeable tilted structure likely due to the ambient wind shear seen in Fig. 13e. Schlatter (2003) asserted that convective storms that formed in a sheared environment can induce spatial offset between the Z_{DR} and K_{DP} columns, and it can be the same for this case given the modest DLS ~ 9.5 m s^{-1} within tornadogenesis time was reported. This is further supported by modelling efforts of dual-polarimetric parameters of Snyder et al. (2017) who found high correlations between the characteristics of K_{DP} columns and the aforementioned supercell updraft properties in an environment composed by sufficient wind shear (such as in a curved hodograph). A small K_{DP} core of ~1.3 $\circ km^{-1}$ was recorded within the radar structure coinciding with high values of Z_H (as discussed before) along the supercell updraft column. This finding is inline to the results of Schlatter (2003) and Kumjian (2013) wherein the K_{DP} column often coincides with the Z_H column, thus composed of high concentration of mixed-phase hydrometeors at various sizes. Furthermore, authors such as Rasmussen and Heymsfield (1987) and Hubbert et al. (1998) noted that this radar signature demarcates the presence of a region of drops shedding off hail due to the high liquid water content and positive temperature perturbation.

Finally, near-surface ρ_{HV} fields (Fig. 13f) reveal a 'ρ_{HV} depression' composed by lowered ρ_{HV} values. These low ρ_{HV} measurements (< 0.80) were likely due to the non-hydrometeor species such as debris being lofted. This further validates the radar scan earlier in Fig. 11 and 12, with the occurrence of TDS/TVS within the area of Magang; including the DRC structure and radial convergence in Fig. 13a and 13b. This is also coincident with the

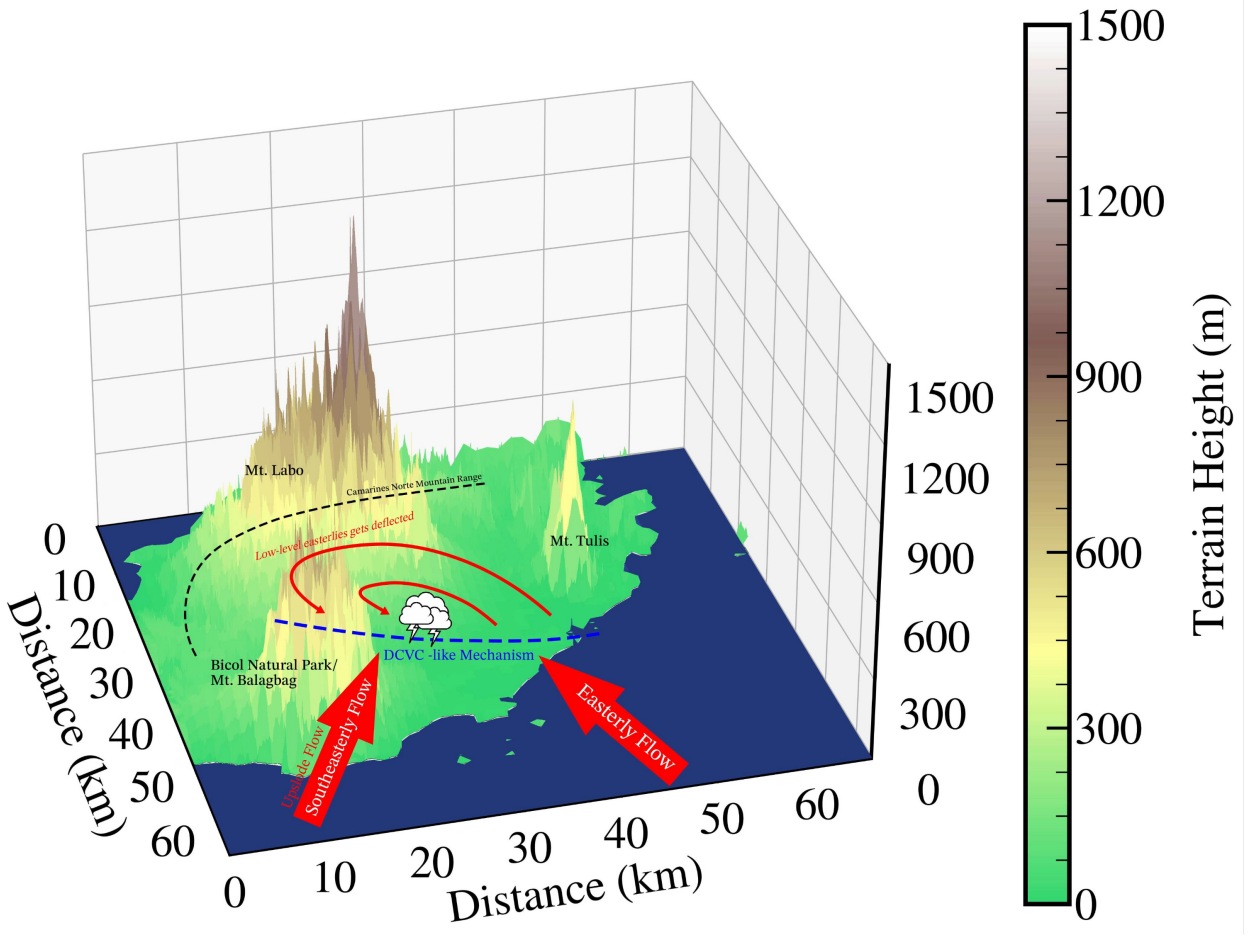


Figure 16. Schematic diagram demonstrating the development of tornadic supercells along Daet, Camarines Norte. Southeasterly wind flow becomes upslope then easterly winds bends backward by the higher terrain forming a vorticity convergence zone similar to DCVC (blue dashed line), hence with thunderstorm icon.

'unusual' Z_{DR} signature along with the tornado-relevant radar parameters discussed earlier where ~1–1.5 dB were recorded which we believe is the signature of the Magang tornado (or its DRC) given its very close distance to the radar site. As indicated, this was unusual, as typical TDS are strongly characterized by near-zero or slightly negative Z_{DR} values due to the chaotic, random orientation of tumbling lofted materials and non-Rayleigh scattering effects from large debris (Broeke 2015; Umeyama et al. 2018). Thus, the observed positive Z_{DR} values may suggest an atypical scenario where heavy precipitation; specifically large, horizontally oblate raindrops with a high dielectric constant, was tightly entrained within the near-surface circulation, overpowering the radar return of the dry debris itself (Kumjian and Ryzhkov 2008; Bodine et al. 2013; Wakimoto et al. 2020).

3) Vertical Cross Section of TS2 (Cahabaan Tornado)

Unlike TS1 and the Magang Tornado (identified as T2 in Section 3.1), TS2 and the Cahabaan Tornado (identified as T3 in Section 3.1) were not recognized at the time of occurrence and remained unreported until the preparation and write up of this study. Despite extensive data scraping efforts for this tornadic supercell, no contemporaneous reports or damage documentation were recovered for this event, limiting opportunities for validation. Nevertheless, based on the radar-derived signatures presented in Section 3.4.1, and considering their apparent association with the localized tornado outbreak, this supercell warrants further examination and discussion.

A vertical slice was retrieved along the tornadic storm that consummated the Cahabaan Tornado from the S-DAT radar. Figure 14 showcases the details of the severe storm's vertical structure, similar to the slice orientation in the Ma-

gang Tornado analysis. A reflectivity maximum of 63 dBZ (solid line, Fig. 14a) extending to ~1.5 km in altitude was observed. The slice of the volume scan reveals the presence of a clear BWER, an indicator of supercell storms and a signature for strong vertical motion. This signature is characterized by an area of low reflectivity surrounded by higher Z_H aloft i.e., echo overhang and the Z_H column which is laterally indicative of an extremely strong updraft that lifts hydrometeors to a significant height. This feature is found in the inflow region of a thunderstorm, similar to the observations conducted by Cotton and Anthes (1989) and Markowski et al. (2002). In fact, BWER is a representative of a local storm that develops in a sheared environment and tends to a steady-state circulation. Similar to TS1, there is also a DRC signature, marked by lowered $Z_H < 51$ dBZ, attached in the rear-flank appendage of the supercell's BWER.

Similar to TS1, the vertical cross section of V_R (Fig. 14b) reveals a distinct mesocyclonic circulation. This TVS becomes particularly pronounced coincident with the timing of tornadogenesis, serving as a classical indicator of intense, low-level cyclonic rotation (French et al. 2013). The localized V_R couplet was concentrated near the surface and extended upward to approximately 1 km. Notably, this circulation was slightly displaced to the west of the DRC. This spatial offset is consistent with established supercell kinematics, where the tornadic circulation typically resides along the strong reflectivity gradient and density boundary adjacent to the RFD and its associated DRC (Rasmussen et al. 2006; Byko et al. 2009). Furthermore, while estimated vertical velocities within the updraft core reached > 3–7 m s^{-1} (Fig. 14c), there was a notable absence of near-surface negative vertical velocity anomalies, a distinct contrast to the structure observed in TS1. This lack of a heavily sampled kinematic downdraft near the surface suggests an updraft-dominated low-level flow regime during this specific volume scan, or indicates that the strongest subsiding parcels of the RFD were positioned outside the immediate sampling plane (Markowski et al. 2002).

As illustrated in Figure 14d, TS2 exhibits a distinct Z_{DR} core and column (~1.5–2 dB), with the highest signal of the Z_{DR} arc (~2.8 dB) also depicted within the sectional slice. Although this overall Z_{DR} signature is slightly less intense than the one observed in TS1, it unambiguously indicates the presence of sparsely distributed, large, highly oblate raindrops. The generation of these large hydrometeors is strongly driven by vigorous warm-rain microphysical processes; specifically rapid collision and coalescence, facilitated by favorable low-level kinematics and rich moisture advection into the convective updraft (e.g., Meischner et al. 1991; Loney et al. 2002, and references therein). Furthermore, the spatial positioning of TS2's Z_{DR} core/column on the inflow flank of the storm, perfectly collocated with the primary updraft interface, is highly consistent with established conceptual models of supercell microphysics and hydrometeor size sorting (Kumjian and Ryzhkov 2008, 2009).

Furthermore, similar to TS1, a K_{DP} column is also present, exhibiting a noticeable tilted structure that is likely induced by the strong ambient vertical wind shear (Fig. 14e). Sufficient vertical wind shear, such as in this case, can induce such tilt and induce a spatial offset between the Z_{DR} and K_{DP} columns (Schlatter 2003; Snyder et al. 2017). While both severe storms feature distinct K_{DP} cores and columns, the K_{DP} signature in TS2 is substantially larger in spatial coverage than in TS1. In TS2, K_{DP} values exceeding ~2.0–2.5 $\circ km^{-1}$ were recorded within the lowest 1 km. This K_{DP} signature, collocated with the low-level updraft and high values in the Z_H column, indicates concentration of liquid water content and composed of high concentration of mixed-phase hydrometeors at various sizes and liquid water content (Schlatter 2003; Kumjian 2013).

Finally, similar to TS1, the near-surface ρ_{HV} fields (Fig. 14f) reveal a distinct 'ρ_{HV} depression'. While these measurements (ranging from 0.70–0.75) are indicative of non-hydrometeors being lofted into the radar volume, they are notably higher than the values observed in TS1 (which dropped as low as 0.34). This discrepancy strongly suggests that the tornadic vortex was primarily lofting lighter, vegetative debris (such as grass, leaves, or light agricultural material) rather than denser structural debris. Polarimetric radar studies that dive to TDS support this interpretation, demonstrating that vegetative debris typically yields higher ρ_{HV} values (between 0.60–0.80) due to its lower dielectric constant and less chaotic scattering properties compared to the highly irregular, highly reflective nature of structural materials like metal, roofing, and fragmented wood (Bodine et al. 2013; Broeke 2015). The presence of this specific debris signature further corroborates the earlier radar analyses (Figs. 11 and 12), which identified a TVS/TDS along Cahabaan. Furthermore, it is consistent with the observed DRC, BWER, and radial convergence presented in Figs. 13a and 13b.

4) Multiparameter Debris Signature Analysis

The evolution of the polarimetric TDS is examined as the tornado affects the town of Magang, Daet. For each time and elevation angle, data is saved within a 1-km radius of the center of the TVS up to 1 km ARL. No reflectivity threshold is imposed to include areas of debris within the weak-echo hole or in areas of adjacent fallout (Griffin et al. 2020).

In Fig. 15a and 15b, the temporal evolution of polarimetric signatures reveals a decrease in both the mean and 90th percentile of Z_H, accompanied by an increase in the mean and 10th percentile of ρ_{HV}, from the onset to the dissipation stage of the debris ball signal after 2220 UTC. These trends suggest that even prior to clear manifestation of TDS/TVS, there is already a discernible increase

in Z_H and corresponding decrease in ρ_{HV}. This behavior is consistent with previously documented polarimetric characteristics of TDS in tornadic storms (e.g., Wakimoto et al. 2025) and aligns with expected scattering responses to enhanced debris concentration and size variability (Cross et al. 2023). During the tornadogenesis phase (2210–2220 UTC), both Z_H and ρ_{HV} exhibit pronounced vertical gradients, with Z_H decreasing and ρ_{HV} increasing with height. This vertical structure is characteristic of debris-laden vortices, where larger and more numerous scatterers are concentrated near the surface. However, by 2220 UTC, a slight reduction in Z_H alongside an increase in ρ_{HV} becomes evident, indicating the initial weakening of the TDS and the subsequent dissipation of the Magang tornado. Quantitatively, the mean $Z_H > 40$ dBZ at 2210 UTC extended up to ~550 mARL, but by 2220 UTC, this height decreased to below 250 mARL. Concurrently, the mean ρ_{HV} increased from ~0.46 at the onset to ~0.61 at 2220 UTC. Similarly, the 10th percentile of ρ_{HV} (< 0.80) reached heights of up to ~600 mARL at 2210 UTC, but decreased to ~450 mARL by 2220 UTC. It is possible that increased low-level debris loading associated with the vortex contributed to this enhancement in low-level debris concentrations. This is similar to Griffin et al. (2020) who found that low-level debris loading may temporarily result in a vertical gradient in polarimetric variables, and the vertical gradient decreases with time if debris lofting is sustained to create a more homogeneous vertical distribution of debris. However, given the lack of Magang tornado documentation, aside from the damage extent, subvortices were not evident in their case.

The vertical structure of the Z_{DR} field exhibits behavior consistent with the observed debris orientations. Mean Z_{DR} (Fig. 15c) is positive and above 1 dB during the times where large debris are evident, and this profile never changed. However, the 25th percentile of mean Z_{DR} by 2210 UTC is closer to zero, than it is in 2220 UTC. Since the mean Z_{DR} is positive, this is indicative that the TDS is mostly comprised of randomly oriented debris and/or hydrometeors that have an offsetting influence on the negative Z_{DR}. However, since there is a relatively small amount of large, airborne debris, negative or positive Z_{DR} associated with visible debris may not heavily influence the mean Z_{DR} in the TDS. Furthermore, TDS can be affected by precipitation entrainment. Bluestein et al. (2007a) observed that precipitation entrainment into the tornado may cause positive Z_{DR} values, despite the low ρ_{HV}, and it can be the same for the Magang Tornado and its associated TDS. Still, local regions of positive or negative Z_{DR} could skew the profile distribution.

To examine the skewness of the Z_{DR} distribution, the Pearson's moment coefficient of skewness is calculated to examine a possible positive or negative skewness of the Z_{DR} distribution during periods of debris alignment (dotted lines; Fig. 15c). The Z_{DR} exhibits some negative skewness in the lowest 200 mARL for most of the period. This is consistent with the low altitudes of the debris that are associated with negative Z_{DR} shown in Fig. 12a6. Between 200–400 mARL, Z_{DR} exhibits positive skewness, even > 400 mARL by 2220 UTC just within the dissipation phase. Wakimoto et al. (2025) asserted that positive skewness would be expected if the debris field contains some large, horizontally oriented scatterers, and these are evident from the lofted roof structures or trees at this time (Fig. 4). Strong vertical motions in the vortex maintain an orientation of the debris that tends to be perpendicular to the wind, consistent with simulations by Umeyama et al. (2018) that found some degree of debris alignment perpendicular to the wind direction (e.g., more horizontal alignment in areas of strong vertical motions). In summary, combining the visible evidence and statistical analysis of the TDS, some degree of common debris alignment appears to occur locally within subregions of the TDS where large debris are present. However, the lack of mean negative Z_{DR} suggests that these scatterers are not present everywhere, at least in this case and may have been affected precipitation entrainment as described by Bluestein et al. (2007a), therefore yielding positive Z_{DR} that lean to small (rayleigh) scatterers instead.

4. SUMMARY AND CONCLUSION

Compared to other tornadic events and SWEs documented in the Philippines over the past decade (Capuli 2024b; Capuli et al. 2026), the 13 September 2025 Camarines Norte tornado outbreak stands out due to both the intensity of its tornadoes reaching up to IF2.5 (EF3-equivalent) and the presence of well-defined, high-quality radar signatures. These characteristics suggest that it is likely one of the most impactful and meteorologically significant tornado outbreaks recorded in the country, despite the limited availability of ground-based documentation.

A major challenge of this study was the limitation in available resources, including accessibility constraints and insufficient personnel, which can hinder the comprehensive assessment of tornado damage and prevented full coverage of all identified tracks (Kingfield and de Beurs 2017). Even in regions such as the United States, where storm damage surveys are routinely conducted, local National Weather Service offices often require several days to document long-track tornadoes. In the Philippine context, these constraints are further amplified, underscoring the need for more systematic and sustained survey efforts. Future tornado documentation would therefore benefit from the organized deployment of survey teams by DOST-PAGASA, equipped with unmanned aerial vehicles (UAVs), to efficiently assess damage over extended periods and across inaccessible areas.

Another key limitation was the absence of photographic documentation for several tornadoes analyzed in this study, including the Magang, Cahabaan, and Napilihan events.

Only the Lag-on tornado had available visual evidence, which restricted the ability to independently verify tornado characteristics and damage indicators for the other cases. This highlights a broader gap in observational data and emphasizes the importance of strengthening documentation practices. Enhancing citizen science initiatives, encouraging public reporting, and improving awareness on proper documentation of severe weather events could significantly augment official datasets. Despite these limitations, this study employed the IF scale to assess tornado intensity, particularly for the Magang tornado, based on the best available damage evidence. While this approach provides a reasonable estimate of tornado strength, improved data collection and documentation efforts in future events will be essential for more robust and reliable damage assessments.

Finally, the absence of high-resolution numerical modeling, such as simulations using the Weather Research and Forecasting (WRF) model or Cloud Model 1 (CM1) could have provided deeper insight into the complex processes governing the tornadic environment. Instead, the analysis relied on available datasets, particularly ERA5 reanalysis, to characterize the large-scale atmospheric conditions. While ERA5 offers valuable meteorological context, its spatial and temporal resolution is insufficient to explicitly resolve storm-scale convection and finer mesoscale features that cloud-resolving models like WRF or CM1 can capture. For instance, Scheffknecht et al. (2017) employed high-resolution modeling to examine the life cycle of a supercell on the northern flank of the Alpine mountain range, demonstrating how the interaction between southwesterly synoptic flow and thermally driven plain-to-mountain circulations created a favorable environment for supercell initiation. Such detailed dynamical processes remain beyond the capability of ERA5. Nevertheless, reanalysis datasets remain robust tools for representing broader synoptic and mesoscale environments. In this study, ERA5 proved essential for characterizing the pre-, during-, and post-storm conditions of the event (around 2210 UTC / 0610 LST), consistent with other severe weather case studies that utilize similar datasets (e.g., Oliveira et al. 2022; Lopes et al. 2025). Future work would benefit from incorporating high-resolution numerical simulations (or even LES modelling) to better resolve tornadic storm dynamics and to more thoroughly assess the role of topography in modulating storm structure and intensity.

This study documents a rare early-morning tornado outbreak in the Bicol Region of the Philippines, associated with an easterly wave (inverted trough) embedded within a moist tropical environment. Synoptic-scale analysis reveals that, despite the absence of strong mid-level forcing, a persistent southeasterly flow regime and a subtle mid-level perturbation supported sustained ascent and moisture transport. The tilted structure of the tropical wave, evident from 850–700 hPa fields, enhanced low-level convergence and vorticity, establishing a favorable background for convective initiation. At the mesoscale, the environment was characterized by moderate instability (CAPE $\sim$ 2000 J kg^{-1}), low LCLs, minimal convective inhibition, and sufficient low-level streamwise vorticity. Although low-level shear remained modest compared to classical tornadic environments, the presence of curved hodographs and enhanced storm-relative helicity supported supercell development. Importantly, terrain-induced effects; particularly flow interaction with the envelope of the elevated terrain in Camarines Norte, likely enhanced low-level convergence and vorticity through mechanisms analogous to a terrain-anchored convergence–vorticity zone. This goes to show that the mesoscale environment may be supportive of supercell development, but tornadogenesis is unlikely to follow unless local modifications to the low-level wind field are present to increase the vorticity and convergence at spatial scales similar to that of the supercell. Topographic configurations can provide the local enhancements of wind shear and static stability that are necessary for tornadogenesis (Bosart et al. 2006). A schematic diagram of the terrain-induced enhancement through the vorticity convergence zone is displayed in Figure 16.

Radar and satellite observations confirmed the presence of multiple embedded supercells within a larger MCS. Satellite analysis revealed intense convective characteristics, including OTs, ACCPs, and extremely cold cloud-top temperatures (< -80 °C), confirming vigorous updrafts capable of supporting severe weather. Lightning analysis indicated a dominance of positive cloud-to-ground flashes, often associated with intense convective systems. Using dual-polarimetric S-DAT radar and its polarimetric variables, three supercells (TS1, TS2, TS3) were identified, three of which produced tornadoes. TS1 (Magang) exhibited a well-defined TDS, strong velocity couplets/TVS, and polarimetric signatures including Z_{DR} arcs, K_{DP} columns, and a DRC feature, consistent with classical tornadic supercell structure. TS2 (Cahabaan) displayed similar but slightly weaker signatures, including a BWER and debris signatures possibly indicative of lighter, vegetative material. The evolution of polarimetric variables in the 'debris ball' of Magang tornado highlighted vertical gradients in Z_H and ρ_{HV}, consistent with debris lofting and subsequent weakening trend. Based on combined damage assessment and radar-derived signatures, the Magang tornado was rated IF2.5 (EF3-equivalent). Both the Cahabaan and Napilihan tornadoes were rated IF1 (EF1-equivalent) identified primarily through radar analysis. In contrast, the Lag-On tornado and a potential landspout detected via S-DAT were rated IF0 (EF0-equivalent) as these were likely brief and traversed over open terrain.

Therefore, this study sought to emphasize and encourage poststorm damage assessments in the Philippines, especially for SWEs. The use of environmental reanalysis, ultra high-resolution satellite imagery (aside from the usual

geostationary satellite), and polarimetric radar have become essential tools to complement ground-level damage surveys, providing crucial information in sparsely populated areas and over forests. If damage analyses such as the one conducted in this study can be expanded, the number of tornado reports in the Philippines can increase significantly and estimates of their intensity can improve, promoting greater knowledge of the climatology of tornadoes in the Philippines.

Acknowledgments. The author expresses sincere gratitude to the Philippine public for reporting the occurrence of the tornado within the affected communities. G. H. Capuli also acknowledges the constructive comments provided by the three anonymous reviewers and the editor, which significantly improved the quality of this manuscript. The author further extends appreciation to Dr. Funing Li of the Massachusetts Institute of Technology (MIT) for valuable guidance related to the use of *xcape*. This work received no funding, but was 'funded' by extensive and exhaustive effort, whose dedication and commitment to advancing our understanding of severe weather phenomena were indispensable. I am thankful to our respective family and loved ones for their unwavering support throughout this research. This work was conducted independently and is presented as a preprint (submitted for publication). Thank you for your understanding.

Author Contribution. **Generich H. Capuli:** Writing - original draft, Writing - review & editing, Visualization, Methodology, Investigation, Formal Analysis, Data curation, Conceptualization, Supervision.

Data availability statement. Data used in this paper were derived from the ERA5 reanalysis (openly available through Climate Data Source), the individual full-disk HIMAWARI-9 Bands were accessible through THREDDS Catalog. The 2023 Philippines Administrative Level 0-4 shapefiles are available in Humanitarian Data Exchange (HDX). The author's associated 1D vertical profile of standard ERA5 model sounding data is archived through Project SWAP and its DR4. The Digital Elevation Model (DEM) is from Copernicus GLO-30 Digital Elevation Model distributed and available in OpenTopography. Finally, the lightning data from the PLDN and radar data are requested through DOST-PAGASA's METTS (Radar), but can also be obtained from the corresponding author upon reasonable request. Proper attribution is required for these datasets.

This paper has made of use of the following Python packages: `Cartopy`, `GeoPandas`, `Matplotlib`, `MetPy`, `NumPy`, `Pandas`, `Rasterio`, `rioxarray`, `SciPy`, `SounderPy`, `xcape`, `PyArt`, `OmniCloudMask`, and `xarray`.

Competing Interest. The author declares no competing interests.

APPENDIX

Supplementary Analysis

Attached in the zip file of this manuscript in arXiv is the Supplementary Damage Analysis related to the Magang Tornado Event.

References

Adams, D. K., and A. C. Comrie, 1997: The North American Monsoon. *Bulletin of the American Meteorological Society*, **78 (10)**, 2197 – 2214, https://doi.org/10.1175/1520-0477(1997)078⟨2197:TNAM⟩2.0.CO;2.

Anderson, C. J., C. K. Wikle, Q. Zhou, and J. A. Royle, 2007: Population Influences on Tornado Reports in the United States. *Weather and Forecasting*, **22 (3)**, 571 – 579, https://doi.org/10.1175/WAF997.1.

Anderson-Frey, A. K., and H. Brooks, 2021: Compared to What? Establishing Environmental Baselines for Tornado Warning Skill. *Bulletin of the American Meteorological Society*, **102 (4)**, E738 – E747, https://doi.org/10.1175/BAMS-D-19-0310.1.

Antonescu, B., H. M. A. M. Ricketts, and D. M. Schultz, 2019: 100 Years Later: Reflecting on Alfred Wegener's Contributions to Tornado Research in Europe. *Bulletin of the American Meteorological Society*, **100 (4)**, 567 – 578, https://doi.org/10.1175/BAMS-D-17-0316.1.

Antonescu, B., D. M. Schultz, A. Holzer, and P. Groenemeijer, 2017: Tornadoes in Europe: An Underestimated Threat. *Bulletin of the American Meteorological Society*, **98 (4)**, 713 – 728, https://doi.org/10.1175/BAMS-D-16-0171.1.

Ashley, W. S., A. M. Haberlie, and J. Strohm, 2019: A Climatology of Quasi-Linear Convective Systems and Their Hazards in the United States. *Weather and Forecasting*, **34 (6)**, 1605 – 1631, https://doi.org/10.1175/WAF-D-19-0014.1.

Atlas, D., R. C. Srivastava, and R. S. Sekhon, 1973: Doppler radar characteristics of precipitation at vertical incidence. *Reviews of Geophysics*, **11 (1)**, 1–35, https://doi.org/https://doi.org/10.1029/RG011i001p00001.

Bagaglini, L., R. Ingrosso, and M. M. Miglietta, 2021: Synoptic patterns and mesoscale precursors of Italian tornadoes. *Atmospheric Research*, **253**, 105 503, https://doi.org/10.1016/j.atmosres.2021.105503.

Bedka, K., J. Brunner, R. Dworak, W. Feltz, J. Otkin, and T. Greenwald, 2010: Objective Satellite-Based Detection of Overshooting Tops Using Infrared Window Channel Brightness Temperature Gradients. *Journal of Applied Meteorology and Climatology*, **49 (2)**, 181 – 202, https://doi.org/10.1175/2009JAMC2286.1.

Bedka, K., E. M. Murillo, C. R. Homeyer, B. Scarino, and H. Mersiovsky, 2018: The above-anvil cirrus plume: An important severe weather indicator in visible and infrared satellite imagery. *Weather and Forecasting*, **33 (5)**, 1159 – 1181, https://doi.org/10.1175/WAF-D-18-0040.1.

Bedka, K. M., C. Wang, R. Rogers, L. D. Carey, W. Feltz, and J. Kanak, 2015: Examining deep convective cloud evolution using total lightning, wsr-88d, and goes-14 super rapid scan datasets*.

Weather and Forecasting, **30 (3)**, 571 – 590, https://doi.org/10.1175/WAF-D-14-00062.1.

Bessho, K., and Coauthors, 2016: An Introduction to Himawari-8/9; Japan's New-Generation Geostationary Meteorological Satellites. *Journal of the Meteorological Society of Japan. Ser. II*, **94 (2)**, 151–183, https://doi.org/10.2151/jmsj.2016-009.

Blanchard, D. O., 2011: Supercells in Environments with Atypical Hodographs. *Weather and Forecasting*, **26 (6)**, 1075 – 1083, https://doi.org/10.1175/WAF-D-11-00012.1.

Bluestein, H. B., M. M. French, R. L. Tanamachi, S. Frasier, K. Hardwick, F. Junyent, and A. L. Pazmany, 2007a: Close-Range Observations of Tornadoes in Supercells Made with a Dual-Polarization, X-Band, Mobile Doppler Radar. *Monthly Weather Review*, **135 (4)**, 1522 – 1543, https://doi.org/10.1175/MWR3349.1.

Bluestein, H. B., C. C. Weiss, M. M. French, E. M. Holthaus, R. L. Tanamachi, S. Frasier, and A. L. Pazmany, 2007b: The Structure of Tornadoes near Attica, Kansas, on 12 May 2004: High-Resolution, Mobile, Doppler Radar Observations. *Monthly Weather Review*, **135 (2)**, 475 – 506, https://doi.org/10.1175/MWR3295.1.

Bodine, D. J., M. R. Kumjian, R. D. Palmer, P. L. Heinselman, and A. V. Ryzhkov, 2013: Tornado damage estimation using polarimetric radar. *Weather and Forecasting*, **28 (1)**, 139 – 158, https://doi.org/10.1175/WAF-D-11-00158.1.

Bosart, L. F., A. Seimon, K. D. LaPenta, and M. J. Dickinson, 2006: Supercell tornadogenesis over complex terrain: The great barrington, massachusetts, tornado on 29 may 1995. *Weather and Forecasting*, **21 (6)**, 897 – 922, https://doi.org/10.1175/WAF957.1.

Boustead, J. M., B. E. Mayes, W. Gargan, J. L. Leighton, G. Phillips, and P. N. Schumacher, 2013: Discriminating Environmental Conditions for Significant Warm Sector and Boundary Tornadoes in Parts of the Great Plains. *Weather and Forecasting*, **28 (6)**, 1498 – 1523, https://doi.org/10.1175/WAF-D-12-00102.1.

Brannan, A. L., and E. R. Martin, 2019: Future characteristics of African Easterly Wave tracks. *Climate Dynamics*, **52**, 5567–5584, https://doi.org/10.1007/s00382-018-4465-z.

Broeke, M. S. V. D., 2015: Polarimetric tornadic debris signature variability and debris fallout signatures. *Journal of Applied Meteorology and Climatology*, **54 (12)**, 2389 – 2405, https://doi.org/10.1175/JAMC-D-15-0077.1.

Broeke, M. S. V. D., 2020: A Preliminary Polarimetric Radar Comparison of Pretornadic and Nontornadic Supercell Storms. *Monthly Weather Review*, **148 (4)**, 1567 – 1584, https://doi.org/10.1175/MWR-D-19-0296.1.

Brooks, H. E., C. A. Doswell, and M. P. Kay, 2003: Climatological estimates of local daily tornado probability for the united states. *Weather and Forecasting*, **18 (4)**, 626 – 640, https://doi.org/10.1175/1520-0434(2003)018⟨0626:CEOLDT⟩2.0.CO;2.

Brown, R. A., and V. T. Wood, 2012: The Tornadic Vortex Signature: An Update. *Weather and Forecasting*, **27 (2)**, 525 – 530, https://doi.org/10.1175/WAF-D-11-00111.1.

Bunkers, M. J., J. S. Johnson, L. J. Czepyha, J. M. Grzywacz, B. A. Klimowski, and M. R. Hjelmfelt, 2006: An Observational Examination of Long-Lived Supercells. Part II: Environmental Conditions and Forecasting. *Weather and Forecasting*, **21 (5)**, 689 – 714, https://doi.org/10.1175/WAF952.1.

Bunkers, M. J., B. A. Klimowski, J. W. Zeitler, R. L. Thompson, and M. L. Weisman, 2000: Predicting Supercell Motion Using a New Hodograph Technique. *Weather and Forecasting*, **15 (1)**, 61 – 79, https://doi.org/10.1175/1520-0434(2000)015⟨0061:PSMUAN⟩2.0.CO;2.

Burow, D., H. V. Herrero, and K. N. Ellis, 2020: Damage Analysis of Three Long-Track Tornadoes Using High-Resolution Satellite Imagery. *Atmosphere*, **11 (6)**, https://doi.org/10.3390/atmos11060613.

Byko, Z., P. Markowski, Y. Richardson, J. Wurman, and E. Adlerman, 2009: Descending Reflectivity Cores in Supercell Thunderstorms Observed by Mobile Radars and in a High-Resolution Numerical Simulation. *Weather and Forecasting*, **24 (1)**, 155 – 186, https://doi.org/10.1175/2008WAF2222116.1.

Capuli, G. H., 2024a: Project Severe Weather Archive of the Philippines (SWAP). Part 1: Establishing a Baseline Climatology for Severe Weather across the Philippine Archipelago. *Annals of Geophysics*, **67 (5)**, GC554, https://doi.org/10.4401/ag-9151.

Capuli, G. H., 2024b: Severe Weather Analysis of Tornado (SWAT): Synoptic and Convective Setting of EF1 Manila Tornado (14 August 2016) over Philippines. [Undergraduate Thesis] Rizal Technological University, https://doi.org/10.13140/RG.2.2.18973.12005.

Capuli, G. H., 2025: Friday the 13th Hailstorm in the Province of Bulacan, Philippines (13 August 2021): A Case Study. *Asia-Pacific Journal of Atmospheric Sciences*, **61 (2)**, 13, https://doi.org/10.1007/s13143-025-00396-6.

Capuli, G. H., M. A. O. Noveno, and M. P. A. Ibañez, 2026: A Case Study of the Tornadic Supercell in the Province of Pampanga, Philippines (27 May 2024). *Natural Hazards*, **122**, 89, https://doi.org/10.1007/s11069-025-07915-8.

Carvalho, L. M. V., and C. Jones, 2001: A Satellite Method to Identify Structural Properties of Mesoscale Convective Systems Based on the Maximum Spatial Correlation Tracking Technique (MASCOTTE). *Journal of Applied Meteorology*, **40 (10)**, 1683 – 1701, https://doi.org/10.1175/1520-0450(2001)040⟨1683:ASMTIS⟩2.0.CO;2.

Caylor, I. J., and A. J. Illingworth, 1987: Radar observations and modelling of warm rain initiation. *Quarterly Journal of the Royal Meteorological Society*, **113 (478)**, 1171–1191, https://doi.org/https://doi.org/10.1002/qj.49711347806.

Choo, S., K.-H. Min, K.-E. Kim, and G. Lee, 2018: A Case Study of Tsukuba Tornado in Japan on 6 May 2012. *J. Korean Earth Sci. Soc.*, **39 (5)**, 403–418, https://doi.org/10.5467/JKESS.2018.39.5.403.

Clark, M. R., 2024: Polarimetric radar observations of the Jersey tornadic supercell on 1–2 November 2023. *Weather*, **79 (11)**, 362–372, https://doi.org/https://doi.org/10.1002/wea.7619.

Coffer, B. E., and M. D. Parker, 2017: Simulated Supercells in Nontornadic and Tornadic VORTEX2 Environments. *Monthly Weather Review*, **145 (1)**, 149 – 180, https://doi.org/10.1175/MWR-D-16-0226.1.

Coffer, B. E., M. D. Parker, J. M. Peters, and A. R. Wade, 2023: Supercell Low-Level Mesocyclones: Origins of Inflow and Vorticity. *Monthly Weather Review*, **151 (9)**, 2205 – 2232, https://doi.org/10.1175/MWR-D-22-0269.1.

Coffer, B. E., M. D. Parker, R. L. Thompson, B. T. Smith, and R. E. Jewell, 2019: Using Near-Ground Storm Relative Helicity in Supercell

Tornado Forecasting. *Weather and Forecasting*, **34 (5)**, 1417 – 1435, https://doi.org/10.1175/WAF-D-19-0115.1.

Coffer, B. E., M. Taszarek, and M. D. Parker, 2020: Near-Ground Wind Profiles of Tornadic and Nontornadic Environments in the United States and Europe from ERA5 Reanalyses. *Weather and Forecasting*, **35 (6)**, 2621 – 2638, https://doi.org/10.1175/WAF-D-20-0153.1.

Coniglio, M. C., and M. D. Parker, 2020: Insights into Supercells and Their Environments from Three Decades of Targeted Radiosonde Observations. *Monthly Weather Review*, **148 (12)**, 4893 – 4915, https://doi.org/10.1175/MWR-D-20-0105.1.

Conway, J. W., and D. S. Zrnić, 1993: A study of embryo production and hail growth using dual-doppler and multiparameter radars. *Monthly Weather Review*, **121 (9)**, 2511 – 2528, https://doi.org/10.1175/1520-0493(1993)121⟨2511:ASOEPA⟩2.0.CO;2.

Cotton, W. R., and R. A. Anthes, 1989: *Storm and Cloud Dynamics*, International Geophysics Series, Vol. 44. Academic Press, San Diego, CA, 883 pp.

Cross, R. N., and Coauthors, 2023: Exploring tornadic debris signature hypotheses using radar simulations and large-eddy simulations. *Journal of Atmospheric and Oceanic Technology*, **40 (10)**, 1199 – 1219, https://doi.org/10.1175/JTECH-D-22-0141.1.

Davies-Jones, R., 1984: Streamwise Vorticity: The Origin of Updraft Rotation in Supercell Storms. *Journal of Atmospheric Sciences*, **41 (20)**, 2991 – 3006, https://doi.org/10.1175/1520-0469(1984)041⟨2991:SVTOOU⟩2.0.CO;2.

Davies-Jones, R., 2015: A review of supercell and tornado dynamics. *Atmospheric Research*, **158-159**, 274–291, https://doi.org/10.1016/j.atmosres.2014.04.007.

Dial, G. L., J. P. Racy, and R. L. Thompson, 2010: Short-Term Convective Mode Evolution along Synoptic Boundaries. *Weather and Forecasting*, **25 (5)**, 1430 – 1446, https://doi.org/10.1175/2010WAF2222315.1.

Dias, M. A. F. S., 2011: An Increase in the Number of Tornado Reports in Brazil. *Weather, Climate, and Society*, **3 (3)**, 209 – 217, https://doi.org/10.1175/2011WCAS1095.1.

Diederich, M., A. Ryzhkov, C. Simmer, P. Zhang, and S. Trömel, 2015: Use of Specific Attenuation for Rainfall Measurement at X-Band Radar Wavelengths. Part II: Rainfall Estimates and Comparison with Rain Gauges. *Journal of Hydrometeorology*, **16 (2)**, 503 – 516, https://doi.org/10.1175/JHM-D-14-0067.1.

Doswell, C. A., and L. F. Bosart, 2001: *Extratropical Synoptic-Scale Processes and Severe Convection*, 27–69. American Meteorological Society, Boston, MA, https://doi.org/10.1007/978-1-935704-06-5_2.

Dowell, D. C., C. R. Alexander, J. M. Wurman, and L. J. Wicker, 2005: Centrifuging of Hydrometeors and Debris in Tornadoes: Radar-Reflectivity Patterns and Wind-Measurement Errors. *Monthly Weather Review*, **133 (6)**, 1501 – 1524, https://doi.org/10.1175/MWR2934.1.

Dowell, D. C., and H. B. Bluestein, 2002: The 8 June 1995 McLean, Texas, Storm. Part II: Cyclic Tornado Formation, Maintenance, and Dissipation. *Monthly Weather Review*, **130 (11)**, 2649 – 2670, https://doi.org/10.1175/1520-0493(2002)130⟨2649:TJMTSP⟩2.0.CO;2.

Dyer, R. C., 1988: Remote sensing identification of tornado tracks in Argentina, Brazil and Paraguay. *Photogrammetric Engineering and Remote Sensing*, **54**, 1429–1435.

Elless, T. J., and R. D. Torn, 2019: Investigating the Factors That Contribute to African Easterly Wave Intensity Forecast Uncertainty in the ECMWF Ensemble Prediction System. *Monthly Weather Review*, **147 (5)**, 1679 – 1698, https://doi.org/10.1175/MWR-D-18-0071.1.

Emanuel, K., 1994: *Atmospheric Convection*. Oxford University Press.

Esterheld, J. M., and D. J. Giuliano, 2008: Discriminating between Tornadic and Non-Tornadic Supercells: A New Hodograph Technique. *Electron. J. Sev. Storms Meteorol.*, **3 (2)**, 1–50, https://doi.org/10.55599/ejssm.v3i2.15.

Evans, J. S., and C. A. Doswell, 2001: Examination of Derecho Environments Using Proximity Soundings. *Weather and Forecasting*, **16 (3)**, 329 – 342, https://doi.org/10.1175/1520-0434(2001)016⟨0329:EODEUP⟩2.0.CO;2.

Feldmann, M., U. Germann, M. Gabella, and A. Berne, 2021: A characterisation of Alpine mesocyclone occurrence. *Weather and Climate Dynamics*, **2 (4)**, 1225–1244, https://doi.org/10.5194/wcd-2-1225-2021.

French, M. M., H. B. Bluestein, I. PopStefanija, C. A. Baldi, and R. T. Bluth, 2013: Reexamining the vertical development of tornadic vortex signatures in supercells. *Monthly Weather Review*, **141 (12)**, 4576 – 4601, https://doi.org/10.1175/MWR-D-12-00315.1.

French, M. M., D. W. Burgess, E. R. Mansell, and L. J. Wicker, 2015: Bulk Hook Echo Raindrop Sizes Retrieved Using Mobile, Polarimetric Doppler Radar Observations. *Journal of Applied Meteorology and Climatology*, **54 (2)**, 423 – 450, https://doi.org/10.1175/JAMC-D-14-0171.1.

Fujita, T. T., 1981: Tornadoes and Downbursts in the Context of Generalized Planetary Scales. *Journal of Atmospheric Sciences*, **38 (8)**, 1511 – 1534, https://doi.org/10.1175/1520-0469(1981)038⟨1511:TADITC⟩2.0.CO;2.

Gillett, K. J., 2025: Sounderpy: An atmospheric sounding visualization and analysis tool for python. *Journal of Open Source Software*, **10 (112)**, 8087, https://doi.org/10.21105/joss.08087.

Griffin, C. B., D. J. Bodine, and R. Palmer, 2020: Polarimetric radar observations of simultaneous tornadoes on 10 may 2010 near norman, oklahoma. *Monthly Weather Review*, **148 (2)**, 477 – 497, https://doi.org/10.1175/MWR-D-19-0156.1.

Groenemeijer, P., A. M. Holzer, T. Kühne, and T. Púčik, 2023: The international fujita (if) scale for tornado and wind damage assessments. Tech. rep., European Severe Storms Laboratory (ESSL), 77 pp. URL https://www.essl.org/cms/wp-content/uploads/IF-scale_v1.0e.pdf.

Groenemeijer, P., and T. Kühne, 2014: A Climatology of Tornadoes in Europe: Results from the European Severe Weather Database. *Monthly Weather Review*, **142 (12)**, 4775 – 4790, https://doi.org/10.1175/MWR-D-14-00107.1.

Grünwald, S., and H. Brooks, 2011: Relationship between sounding derived parameters and the strength of tornadoes in europe and the usa from reanalysis data. *Atmospheric Research*, **100 (4)**, 479–488, https://doi.org/10.1016/j.atmosres.2010.11.011.

Helmus, J. J., and S. M. Collis, 2016: The Python ARM Radar Toolkit (Py-ART), a Library for Working with Weather Radar Data in the Python Programming Language. *Journal of Open Research Software*, **4 (1)**, https://doi.org/10.5334/jors.119.

Hengstebeck, T., K. Wapler, D. Heizenreder, and P. Joe, 2018: Radar Network–Based Detection of Mesocyclones at the German Weather

Service. *Journal of Atmospheric and Oceanic Technology*, **35 (2)**, 299 – 321, https://doi.org/10.1175/JTECH-D-16-0230.1.

Hersbach, H., and Coauthors, 2020: The ERA5 global reanalysis. *Quarterly Journal of the Royal Meteorological Society*, **146 (730)**, 1999–2049, https://doi.org/10.1002/qj.3803.

Hirose, H., S. Shige, M. K. Yamamoto, and A. Higuchi, 2019: High Temporal Rainfall Estimations from Himawari-8 Multiband Observations Using the Random-Forest Machine-Learning Method. *Journal of the Meteorological Society of Japan. Ser. II*, **97 (3)**, 689–710, https://doi.org/10.2151/jmsj.2019-040.

Homeyer, C. R., T. N. Sandmæl, C. K. Potvin, and A. M. Murphy, 2020: Distinguishing Characteristics of Tornadic and Nontornadic Supercell Storms from Composite Mean Analyses of Radar Observations. *Monthly Weather Review*, **148 (12)**, 5015 – 5040, https://doi.org/10.1175/MWR-D-20-0136.1.

Hoque, M. A.-A., S. Phinn, C. Roelfsema, and I. Childs, 2017: Tropical cyclone disaster management using remote sensing and spatial analysis: A review. *International Journal of Disaster Risk Reduction*, **22**, 345–354, https://doi.org/10.1016/j.ijdrr.2017.02.008.

Howard, J., and S. Gugger, 2020: Fastai: A Layered API for Deep Learning. *Information*, **11 (2)**, https://doi.org/10.3390/info11020108.

Hubbert, J., V. N. Bringi, L. D. Carey, and S. Bolen, 1998: Csuchill polarimetric radar measurements from a severe hail storm in eastern colorado. *Journal of Applied Meteorology*, **37 (8)**, 749 – 775, https://doi.org/10.1175/1520-0450(1998)037⟨0749:CCPRMF⟩2.0.CO;2.

Jiang, Q., D. T. Dawson II, F. Li, and D. R. Chavas, 2025: Classifying synoptic patterns driving tornadic storms and associated spatial trends in the united states. *npj Climate and Atmospheric Science*, **8**, 7, https://doi.org/10.1038/s41612-025-00897-1.

Kilambi, A., F. Fabry, and V. Meunier, 2018: A Simple and Effective Method for Separating Meteorological from Nonmeteorological Targets Using Dual-Polarization Data. *Journal of Atmospheric and Oceanic Technology*, **35 (7)**, 1415 – 1424, https://doi.org/10.1175/JTECH-D-17-0175.1.

King, A. T., and A. D. Kennedy, 2019: North American Supercell Environments in Atmospheric Reanalyses and RUC-2. *Journal of Applied Meteorology and Climatology*, **58 (1)**, 71 – 92, https://doi.org/10.1175/JAMC-D-18-0015.1.

Kingfield, D. M., and K. M. de Beurs, 2017: Landsat identification of tornado damage by land cover and an evaluation of damage recovery in forests. *Journal of Applied Meteorology and Climatology*, **56 (4)**, 965 – 987, https://doi.org/10.1175/JAMC-D-16-0228.1.

Kirshbaum, D. J., B. Adler, N. Kalthoff, C. Barthlott, and S. Serafin, 2018: Moist Orographic Convection: Physical Mechanisms and Links to Surface-Exchange Processes. *Atmosphere*, **9 (3)**, https://doi.org/10.3390/atmos9030080.

Klemp, J. B., and R. Rotunno, 1983: A Study of the Tornadic Region within a Supercell Thunderstorm. *Journal of Atmospheric Sciences*, **40 (2)**, 359 – 377, https://doi.org/10.1175/1520-0469(1983)040⟨0359:ASOTTR⟩2.0.CO;2.

Kumjian, M. R., 2013: Principles and applications of dual-polarization weather radar. Part I: Description of the polarimetric radar variables. *Journal of Operational Meteorology*, **1 (19)**, 226–242, https://doi.org/10.15191/nwajom.2013.0119.

Kumjian, M. R., and A. V. Ryzhkov, 2008: Polarimetric Signatures in Supercell Thunderstorms. *Journal of Applied Meteorology and Climatology*, **47 (7)**, 1940 – 1961, https://doi.org/10.1175/2007JAMC1874.1.

Kumjian, M. R., and A. V. Ryzhkov, 2009: Storm-Relative Helicity Revealed from Polarimetric Radar Measurements. *Journal of the Atmospheric Sciences*, **66 (3)**, 667 – 685, https://doi.org/10.1175/2008JAS2815.1.

Lee, S.-K., R. Atlas, D. Enfield, C. Wang, and H. Liu, 2013: Is There an Optimal ENSO Pattern That Enhances Large-Scale Atmospheric Processes Conducive to Tornado Outbreaks in the United States? *Journal of Climate*, **26 (5)**, 1626 – 1642, https://doi.org/10.1175/JCLI-D-12-00128.1.

Lepore, C., J. Allen, and R. Abernathey, 2021: xcape (v0.1.4). Zenodo, URL https://doi.org/10.5281/zenodo.5270332, https://doi.org/10.5281/zenodo.5270332.

León-Cruz, J. F., 2025: Tornadic environments in mexico. *Atmospheric Research*, **315**, 107 916, https://doi.org/10.1016/j.atmosres.2025.107916.

León-Cruz, J. F., L. F. Pineda-Martínez, and N. Carbajal, 2022: Tornado climatology and potentially severe convective environments in Mexico. *Climate Research*, **87**, 147–165, https://doi.org/10.3354/cr01692.

Lin, P.-F., L. K. M. Lagrimas, J.-B. Wang, P.-L. Chang, W.-T. Fang, J. G. C. Almario, B. J.-D. Jou, and E. O. Cayanan, 2021: Removing interference echoes in Philippine radars using a fuzzy logic approach. *Terr. Atmos. Ocean. Sci.*, **32 (5.1)**, 755–776, https://doi.org/10.3319/TAO.2021.12.20.01.

Loney, M. L., D. S. Zrnić, J. M. Straka, and A. V. Ryzhkov, 2002: Enhanced polarimetric radar signatures above the melting level in a supercell storm. *Journal of Applied Meteorology*, **41 (12)**, 1179 – 1194, https://doi.org/10.1175/1520-0450(2002)041⟨1179:EPRSAT⟩2.0.CO;2.

Lopes, M. M., M. I. de Oliveira, V. Goede, V. Ferreira, and E. de Lima Nascimento, 2025: Damage Survey and Multisensor Analysis of a Cold Season Tornado Outbreak in Southern Brazil. *Journal of Applied Meteorology and Climatology*, **64 (7)**, 831 – 855, https://doi.org/10.1175/JAMC-D-24-0146.1.

Markowski, P., C. Hannon, J. Frame, E. Lancaster, A. Pietrycha, R. Edwards, and R. L. Thompson, 2003: Characteristics of Vertical Wind Profiles near Supercells Obtained from the Rapid Update Cycle. *Weather and Forecasting*, **18 (6)**, 1262 – 1272, https://doi.org/10.1175/1520-0434(2003)018⟨1262:COVWPN⟩2.0.CO;2.

Markowski, P., and Y. Richardson, 2010: *Mesoscale Meteorology in Midlatitudes*. John Wiley & Sons, https://doi.org/10.1002/9780470682104.

Markowski, P. M., J. M. Straka, and E. N. Rasmussen, 2002: Direct surface thermodynamic observations within the rear-flank downdrafts of nontornadic and tornadic supercells. *Monthly Weather Review*, **130 (7)**, 1692 – 1721, https://doi.org/10.1175/1520-0493(2002)130⟨1692:DSTOWT⟩2.0.CO;2.

Matsui, T., J.-D. Chern, W.-K. Tao, S. Lang, M. Satoh, T. Hashino, and T. Kubota, 2016: On the Land–Ocean Contrast of Tropical Convection and Microphysics Statistics Derived from TRMM Satellite Signals and Global Storm-Resolving Models. *Journal of Hydrometeorology*, **17 (5)**, 1425 – 1445, https://doi.org/10.1175/JHM-D-15-0111.1.

Meischner, P. F., V. N. Bringi, D. Heimann, and H. Höller, 1991: A squall line in southern germany: Kinematics and precipitation formation as deduced by advanced polarimetric and doppler radar measurements. *Monthly Weather Review*, **119 (3)**, 678 – 701, https://doi.org/10.1175/1520-0493(1991)119⟨0678:ASLISG⟩2.0.CO;2.

Mercer, A. E., C. M. Shafer, C. A. Doswell, L. M. Leslie, and M. B. Richman, 2012: Synoptic Composites of Tornadic and Nontornadic Outbreaks. *Monthly Weather Review*, **140 (8)**, 2590 – 2608, https://doi.org/10.1175/MWR-D-12-00029.1.

Nielsen, E. R., and R. S. Schumacher, 2018: Dynamical insights into extreme short-term precipitation associated with supercells and mesovortices. *Journal of the Atmospheric Sciences*, **75 (9)**, 2983 – 3009, https://doi.org/10.1175/JAS-D-17-0385.1.

Nielsen, E. R., and R. S. Schumacher, 2020: Dynamical mechanisms supporting extreme rainfall accumulations in the houston "tax day" 2016 flood. *Monthly Weather Review*, **148 (1)**, 83 – 109, https://doi.org/10.1175/MWR-D-19-0206.1.

Nixon, C. J., and J. T. Allen, 2021: Anticipating Deviant Tornado Motion Using a Simple Hodograph Technique. *Weather and Forecasting*, **36 (1)**, 219 – 235, https://doi.org/10.1175/WAF-D-20-0056.1.

Nixon, C. J., and J. T. Allen, 2022: Distinguishing between Hodographs of Severe Hail and Tornadoes. *Weather and Forecasting*, **37 (10)**, 1761 – 1782, https://doi.org/10.1175/WAF-D-21-0136.1.

Nixon, C. J., J. T. Allen, M. B. Wilson, M. J. Bunkers, and M. Taszarek, 2024: Cell Mergers, Boundary Interactions, and Convective Systems in Cases of Significant Tornadoes and Hail. *Weather and Forecasting*, **39 (10)**, 1435 – 1458, https://doi.org/10.1175/WAF-D-23-0117.1.

Nowotarski, C. J., and E. A. Jones, 2018: Multivariate Self-Organizing Map Approach to Classifying Supercell Tornado Environments Using Near-Storm, Low-Level Wind and Thermodynamic Profiles. *Weather and Forecasting*, **33 (3)**, 661 – 670, https://doi.org/10.1175/WAF-D-17-0189.1.

Oliveira, M. I., F. S. Puhales, E. L. Nascimento, and V. Anabor, 2022: Integrated damage, visual, remote sensing, and environmental analysis of a strong tornado in southern Brazil. *Atmospheric Research*, **274**, 106 188, https://doi.org/10.1016/j.atmosres.2022.106188.

Orf, L., R. Wilhelmson, B. Lee, C. Finley, and A. Houston, 2017: Evolution of a Long-Track Violent Tornado within a Simulated Supercell. *Bulletin of the American Meteorological Society*, **98 (1)**, 45 – 68, https://doi.org/10.1175/BAMS-D-15-00073.1.

Overeem, A., R. Uijlenhoet, and H. Leijnse, 2020: Full-Year Evaluation of Nonmeteorological Echo Removal with Dual-Polarization Fuzzy Logic for Two C-Band Radars in a Temperate Climate. *Journal of Atmospheric and Oceanic Technology*, **37 (9)**, 1643 – 1660, https://doi.org/10.1175/JTECH-D-19-0149.1.

Peters, J. M., D. R. Chavas, C.-Y. Su, H. Morrison, and B. E. Coffer, 2023: An Analytic Formula for Entraining CAPE in Midlatitude Storm Environments. *Journal of the Atmospheric Sciences*, **80 (9)**, 2165 – 2186, https://doi.org/10.1175/JAS-D-23-0003.1.

Peters, J. M., W. Hannah, and H. Morrison, 2019: The Influence of Vertical Wind Shear on Moist Thermals. *Journal of the Atmospheric Sciences*, **76 (6)**, 1645 – 1659, https://doi.org/10.1175/JAS-D-18-0296.1.

Peters, J. M., H. Morrison, T. C. Nelson, J. N. Marquis, J. P. Mulholland, and C. J. Nowotarski, 2022a: The influence of shear on deep convection initiation. part i: Theory. *Journal of the Atmospheric Sciences*, **79 (6)**, 1669 – 1690, https://doi.org/10.1175/JAS-D-21-0145.1.

Peters, J. M., H. Morrison, T. C. Nelson, J. N. Marquis, J. P. Mulholland, and C. J. Nowotarski, 2022b: The influence of shear on deep convection initiation. part ii: Simulations. *Journal of the Atmospheric Sciences*, **79 (6)**, 1691 – 1711, https://doi.org/10.1175/JAS-D-21-0144.1.

Peters, J. M., J. P. Mulholland, and D. R. Chavas, 2022c: Generalized Lapse Rate Formulas for Use in Entraining CAPE Calculations. *Journal of the Atmospheric Sciences*, **79 (3)**, 815 – 836, https://doi.org/10.1175/JAS-D-21-0118.1.

Picca, J., M. Kumjian, and A. Ryzhkov, 2010: ZDR columns as a predictive tool for hail growth and storm evolution. *25th Conference on Severe Local Storms*, Denver, CO, American Meteorological Society, URL https://ams.confex.com/ams/25SLS/techprogram/paper_175750.htm, paper 11.3.

Pilguj, N., M. Taszarek, J. T. Allen, and K. A. Hoogewind, 2022a: Are Trends in Convective Parameters over the United States and Europe Consistent between Reanalyses and Observations? *Journal of Climate*, **35 (12)**, 3605 – 3626, https://doi.org/10.1175/JCLI-D-21-0135.1.

Pilguj, N., M. Taszarek, M. Kryza, and H. E. Brooks, 2022b: Reconstruction of Violent Tornado Environments in Europe: High-Resolution Dynamical Downscaling of ERA5. *Geophysical Research Letters*, **49 (11)**, e2022GL098 242, https://doi.org/https://doi.org/10.1029/2022GL098242, https://agupubs.onlinelibrary.wiley.com/doi/pdf/10.1029/2022GL098242.

Planet Team, 2024: Technical specification: Analysis-ready planetscope (arps). Version 1.0.0, October 2024; accessed April 2026, https://docs.planet.com/data/imagery/arps/techspec/.

Púčik, T., P. Groenemeijer, D. Rýva, and M. Kolář, 2015: Proximity Soundings of Severe and Nonsevere Thunderstorms in Central Europe. *Monthly Weather Review*, **143 (12)**, 4805 – 4821, https://doi.org/10.1175/MWR-D-15-0104.1.

Púčik, T., and Coauthors, 2024: The Violent Tornado on 24 June 2021 in Czechia: Damage Survey, Societal Impacts, and Lessons Learned. *Weather, Climate, and Society*, **16 (3)**, 411 – 429, https://doi.org/10.1175/WCAS-D-23-0080.1.

Rasmussen, E. N., 2003: Refined supercell and tornado forecast parameters. *Weather and Forecasting*, **18 (3)**, 530 – 535, https://doi.org/10.1175/1520-0434(2003)18⟨530:RSATFP⟩2.0.CO;2.

Rasmussen, E. N., and D. O. Blanchard, 1998: A Baseline Climatology of Sounding-Derived Supercell and Tornado Forecast Parameters. *Weather and Forecasting*, **13 (4)**, 1148 – 1164, https://doi.org/10.1175/1520-0434(1998)013⟨1148:ABCOSD⟩2A.0.CO;2.

Rasmussen, E. N., J. M. Straka, M. S. Gilmore, and R. Davies-Jones, 2006: A Preliminary Survey of Rear-Flank Descending Reflectivity Cores in Supercell Storms. *Weather and Forecasting*, **21 (6)**, 923 – 938, https://doi.org/10.1175/WAF962.1.

Rasmussen, K. L., A. F. Prein, R. M. Rasmussen, K. Ikeda, and C. Liu, 2020: Changes in the convective population and thermodynamic environments in convection-permitting regional climate simulations over the United States. *Climate Dynamics*, **55 (1)**, 383–408, https://doi.org/10.1007/s00382-017-4000-7.

Rasmussen, R. M., and A. J. Heymsfield, 1987: Melting and shedding of graupel and hail. part ii: Sensitivity study. *Journal of Atmospheric Sciences*, **44 (19)**, 2764 – 2782, https://doi.org/10.1175/1520-0469(1987)044⟨2764:MASOGA⟩2.0.CO;2.

Romps, D. M., and Z. Kuang, 2010: Do Undiluted Convective Plumes Exist in the Upper Tropical Troposphere? *Journal of the Atmospheric Sciences*, **67 (2)**, 468 – 484, https://doi.org/10.1175/2009JAS3184.1.

Ronneberger, O., P. Fischer, and T. Brox, 2015: U-Net: Convolutional Networks for Biomedical Image Segmentation. *Medical Image Computing and Computer-Assisted Intervention – MICCAI 2015*, N. Navab, J. Hornegger, W. M. Wells, and A. F. Frangi, Eds., Springer International Publishing, Cham, 234–241, https://doi.org/10.1007/978-3-319-24574-4_28.

Rossow, W. B., A. Mekonnen, C. Pearl, and W. Goncalves, 2013: Tropical Precipitation Extremes. *Journal of Climate*, **26 (4)**, 1457 – 1466, https://doi.org/10.1175/JCLI-D-11-00725.1.

Ryzhkov, A. V., T. J. Schuur, D. W. Burgess, and D. S. Zrnic, 2005: Polarimetric Tornado Detection. *Journal of Applied Meteorology*, **44 (5)**, 557 – 570, https://doi.org/10.1175/JAM2235.1.

Schaefer, M., R. Teeuw, S. Day, D. Zekkos, P. Weber, T. Meredith, and C. J. van Westen, 2020: Low-cost UAV surveys of hurricane damage in Dominica: automated processing with co-registration of pre-hurricane imagery for change analysis. *Natural Hazards*, **101**, 755–784, https://doi.org/10.1007/s11069-020-03893-1.

Scheffknecht, P., S. Serafin, and V. Grubišić, 2017: A long-lived supercell over mountainous terrain. *Quarterly Journal of the Royal Meteorological Society*, **143 (709)**, 2973–2986, https://doi.org/10.1002/qj.3127.

Schlatter, P. T., 2003: Polarimetric radar and in situ measurements of a hook echo. Master's thesis, University of Oklahoma, School of Meteorology, 97 pp., Norman, OK, available from School of Meteorology, University of Oklahoma, Suite 1310, 100 East Boyd St., Norman, OK 73019.

Schmit, T. J., and Coauthors, 2013: Geostationary Operational Environmental Satellite (GOES)-14 super rapid scan operations to prepare for GOES-R. *Journal of Applied Remote Sensing*, **7 (1)**, 073 462, https://doi.org/10.1117/1.JRS.7.073462.

Schueth, A., C. Weiss, and J. M. L. Dahl, 2021: Comparing Observations and Simulations of the Streamwise Vorticity Current and the Forward-Flank Convergence Boundary in a Supercell Storm. *Monthly Weather Review*, **149 (6)**, 1651 – 1671, https://doi.org/10.1175/MWR-D-20-0251.1.

Schultz, C. J., W. A. Petersen, and L. D. Carey, 2011: Lightning and Severe Weather: A Comparison between Total and Cloud-to-Ground Lightning Trends. *Weather and Forecasting*, **26 (5)**, 744 – 755, https://doi.org/10.1175/WAF-D-10-05026.1.

Schumann, M. R., and P. J. Roebber, 2010: The Influence of Upper-Tropospheric Potential Vorticity on Convective Morphology. *Monthly Weather Review*, **138 (2)**, 463 – 474, https://doi.org/10.1175/2009MWR3091.1.

Schwarz, C. M., and D. W. Burgess, 2011: Supercell polarimetric signatures at X-band: Data from VORTEX2. *35th Conference on Radar Meteorology*, Pittsburgh, PA, American Meteorological Society, URL https://ams.confex.com/ams/35Radar/webprogram/Paper191298.html, paper 7B.4.

Serra, Y. L., G. N. Kiladis, and M. F. Cronin, 2008: Horizontal and vertical structure of easterly waves in the pacific itcz. *Journal of the Atmospheric Sciences*, **65 (4)**, 1266 – 1284, https://doi.org/10.1175/2007JAS2341.1.

Sherburn, K. D., and M. D. Parker, 2014: Climatology and Ingredients of Significant Severe Convection in High-Shear, Low-CAPE Environments. *Weather and Forecasting*, **29 (4)**, 854 – 877, https://doi.org/10.1175/WAF-D-13-00041.1.

Smith, B. T., R. L. Thompson, J. S. Grams, C. Broyles, and H. E. Brooks, 2012: Convective Modes for Significant Severe Thunderstorms in the Contiguous United States. Part I: Storm Classification and Climatology. *Weather and Forecasting*, **27 (5)**, 1114 – 1135, https://doi.org/10.1175/WAF-D-11-00115.1.

Snyder, J. C., H. B. Bluestein, D. T. D. II, and Y. Jung, 2017: Simulations of polarimetric, x-band radar signatures in supercells. part ii: Zdr columns and rings and kdp columns. *Journal of Applied Meteorology and Climatology*, **56 (7)**, 2001 – 2026, https://doi.org/10.1175/JAMC-D-16-0139.1.

Stumpf, G. J., A. Witt, E. D. Mitchell, P. L. Spencer, J. T. Johnson, M. D. Eilts, K. W. Thomas, and D. W. Burgess, 1998: The National Severe Storms Laboratory Mesocyclone Detection Algorithm for the WSR-88D. *Weather and Forecasting*, **13 (2)**, 304 – 326, https://doi.org/10.1175/1520-0434(1998)013⟨0304:TNSSLM⟩2.0.CO;2.

Szoke, E. J., 1991: Eye of the denver cyclone. *Monthly Weather Review*, **119 (5)**, 1283 – 1292, https://doi.org/10.1175/1520-0493(1991)119⟨1283:EOTDC⟩2.0.CO;2.

Tan, J., C. Jakob, and T. P. Lane, 2013: On the Identification of the Large-Scale Properties of Tropical Convection Using Cloud Regimes. *Journal of Climate*, **26 (17)**, 6618 – 6632, https://doi.org/10.1175/JCLI-D-12-00624.1.

Taszarek, M., J. T. Allen, P. Groenemeijer, R. Edwards, H. E. Brooks, V. Chmielewski, and S.-E. Enno, 2020a: Severe Convective Storms across Europe and the United States. Part I: Climatology of Lightning, Large Hail, Severe Wind, and Tornadoes. *Journal of Climate*, **33 (23)**, 10 239 – 10 261, https://doi.org/10.1175/JCLI-D-20-0345.1.

Taszarek, M., J. T. Allen, M. Marchio, and H. E. Brooks, 2021a: Global climatology and trends in convective environments from ERA5 and rawinsonde data. *npj Climate and Atmospheric Science*, **4 (1)**, 35, https://doi.org/10.1038/s41612-021-00190-x.

Taszarek, M., J. T. Allen, T. Púčik, K. A. Hoogewind, and H. E. Brooks, 2020b: Severe Convective Storms across Europe and the United States. Part II: ERA5 Environments Associated with Lightning, Large Hail, Severe Wind, and Tornadoes. *Journal of Climate*, **33 (23)**, 10 263 – 10 286, https://doi.org/10.1175/JCLI-D-20-0346.1.

Taszarek, M., N. Pilguj, J. T. Allen, V. Gensini, H. E. Brooks, and P. Szuster, 2021b: Comparison of Convective Parameters Derived from ERA5 and MERRA-2 with Rawinsonde Data over Europe and North America. *Journal of Climate*, **34 (8)**, 3211 – 3237, https://doi.org/10.1175/JCLI-D-20-0484.1.

Thompson, R. L., and R. Edwards, 2000: An Overview of Environmental Conditions and Forecast Implications of the 3 May 1999 Tornado Outbreak. *Weather and Forecasting*, **15 (6)**, 682 – 699, https://doi.org/10.1175/1520-0434(2000)015⟨0682:AOOECA⟩2.0.CO;2.

Thompson, R. L., R. Edwards, J. A. Hart, K. L. Elmore, and P. Markowski, 2003: Close Proximity Soundings within Supercell Environments Obtained from the Rapid Update Cycle. *Weather and Forecasting*, **18 (6)**, 1243 – 1261, https://doi.org/10.1175/1520-0434(2003)018⟨1243:CPSWSE⟩2.0.CO;2.

Thompson, R. L., B. T. Smith, J. S. Grams, A. R. Dean, and C. Broyles, 2012: Convective Modes for Significant Severe Thunderstorms in

the Contiguous United States. Part II: Supercell and QLCS Tornado Environments. *Weather and Forecasting*, **27 (5)**, 1136 – 1154, https://doi.org/10.1175/WAF-D-11-00116.1.

Trier, S. B., G. S. Romine, D. A. Ahijevych, and R. A. Sobash, 2019: Lower-tropospheric influences on the timing and intensity of afternoon severe convection over modest terrain in a convection-allowing ensemble. *Weather and Forecasting*, **34 (6)**, 1633 – 1656, https://doi.org/10.1175/WAF-D-19-0087.1.

Tuttle, J. D., V. N. Bringi, H. D. Orville, and F. J. Kopp, 1989: Multiparameter radar study of a microburst: Comparison with model results. *Journal of Atmospheric Sciences*, **46 (5)**, 601 – 620, https://doi.org/10.1175/1520-0469(1989)046⟨0601:MRSOAM⟩2.0.CO;2.

Umeyama, A., B. L. Cheong, S. Torres, and D. Bodine, 2018: Orientation analysis of simulated tornadic debris. *Journal of Atmospheric and Oceanic Technology*, **35 (5)**, 993 – 1010, https://doi.org/10.1175/JTECH-D-17-0140.1.

Wagner, M., R. K. Doe, A. Johnson, Z. Chen, J. Das, and R. S. Cerveny, 2019: Unpiloted Aerial Systems (UASs) Application for Tornado Damage Surveys: Benefits and Procedures. *Bulletin of the American Meteorological Society*, **100 (12)**, 2405 – 2409, https://doi.org/10.1175/BAMS-D-19-0124.1.

Wakimoto, R. M., N. T. Atkins, K. M. Butler, H. B. Bluestein, K. Thiem, J. Snyder, and J. Houser, 2015: Photogrammetric Analysis of the 2013 El Reno Tornado Combined with Mobile X-Band Polarimetric Radar Data. *Monthly Weather Review*, **143 (7)**, 2657 – 2683, https://doi.org/10.1175/MWR-D-15-0034.1.

Wakimoto, R. M., N. T. Atkins, and J. Wurman, 2011: The LaGrange Tornado during VORTEX2. Part I: Photogrammetric Analysis of the Tornado Combined with Single-Doppler Radar Data. *Monthly Weather Review*, **139 (7)**, 2233 – 2258, https://doi.org/10.1175/2010MWR3568.1.

Wakimoto, R. M., D. J. Bodine, H. B. Bluestein, T. Greenwood, and S. Emmerson, 2025: Kinematic Structure of a Tornado Based on an Analysis of Lofted Debris Speeds, Debris Orientation, and Mobile Radar Data. *Monthly Weather Review*, **153 (8)**, 1365 – 1383, https://doi.org/10.1175/MWR-D-24-0176.1.

Wakimoto, R. M., H. Cai, and H. V. Murphey, 2004: The Superior, Nebraska, Supercell During BAMEX. *Bulletin of the American Meteorological Society*, **85 (8)**, 1095 – 1106, https://doi.org/10.1175/BAMS-85-8-1095.

Wakimoto, R. M., W.-C. Lee, H. B. Bluestein, C.-H. Liu, and P. H. Hildebrand, 1996: ELDORA Observations during VORTEX 95. *Bulletin of the American Meteorological Society*, **77 (7)**, 1465 – 1482, https://doi.org/10.1175/1520-0477(1996)077⟨1465:EODV⟩2.0.CO;2.

Wakimoto, R. M., Z. Wienhoff, H. B. Bluestein, D. J. Bodine, and J. M. Kurdzo, 2020: Mobile radar observations of the evolving debris field compared with a damage survey of the shawnee, oklahoma, tornado of 19 may 2013. *Monthly Weather Review*, **148 (5)**, 1779 – 1803, https://doi.org/10.1175/MWR-D-19-0215.1.

Wang, X., H. Iwabuchi, and T. Yamashita, 2022: Cloud identification and property retrieval from Himawari-8 infrared measurements via a deep neural network. *Remote Sensing of Environment*, **275**, 113 026, https://doi.org/10.1016/j.rse.2022.113026.

Weisman, M. L., and J. B. Klemp, 1986: *Characteristics of Isolated Convective Storms*, 331–358. American Meteorological Society, Boston, MA, https://doi.org/10.1007/978-1-935704-20-1_15.

Wightman, R., 2019: PyTorch Image Models. GitHub, https://github.com/rwightman/pytorch-image-models, https://doi.org/10.5281/zenodo.4414861.

Wilczak, J. M., D. E. Wolfe, R. J. Zamora, B. Stankov, and T. W. Christian, 1992: Observations of a colorado tornado. part i: Mesoscale environment and tornadogenesis. *Monthly Weather Review*, **120 (4)**, 497 – 521, https://doi.org/10.1175/1520-0493(1992)120⟨0497:OOACTP⟩2.0.CO;2.

Wright, N., J. M. Duncan, J. N. Callow, S. E. Thompson, and R. J. George, 2024: CloudS2Mask: A novel deep learning approach for improved cloud and cloud shadow masking in Sentinel-2 imagery. *Remote Sensing of Environment*, **306**, 114 122, https://doi.org/10.1016/j.rse.2024.114122.

Wurman, J., and S. Gill, 2000: Finescale Radar Observations of the Dimmitt, Texas (2 June 1995), Tornado. *Monthly Weather Review*, **128 (7)**, 2135 – 2164, https://doi.org/10.1175/1520-0493(2000)128⟨2135:FROOTD⟩2.0.CO;2.

Wurman, J., and K. Kosiba, 2013: Finescale Radar Observations of Tornado and Mesocyclone Structures. *Weather and Forecasting*, **28 (5)**, 1157 – 1174, https://doi.org/10.1175/WAF-D-12-00127.1.

Wurman, J., K. Kosiba, T. White, and P. Robinson, 2021: Supercell tornadoes are much stronger and wider than damage-based ratings indicate. *Proceedings of the National Academy of Sciences*, **118 (14)**, e2021535 118, https://doi.org/10.1073/pnas.2021535118.

Wurman, J., J. M. Straka, and E. N. Rasmussen, 1996: Fine-Scale Doppler Radar Observations of Tornadoes. *Science*, **272 (5269)**, 1774–1777, https://doi.org/10.1126/science.272.5269.1774.

Xie, M., N. Jean, M. Burke, D. Lobell, and S. Ermon, 2016: Transfer Learning from Deep Features for Remote Sensing and Poverty Mapping. *Proceedings of the AAAI Conference on Artificial Intelligence*, **30 (1)**, https://doi.org/10.1609/aaai.v30i1.9906.

Xu, K.-M., and K. A. Emanuel, 1989: Is the Tropical Atmosphere Conditionally Unstable? *Monthly Weather Review*, **117 (7)**, 1471 – 1479, https://doi.org/10.1175/1520-0493(1989)117⟨1471:ITTACU⟩2.0.CO;2.

Yuan, C., Y. Bai, P. Sun, H. Bai, and L. Xia, 2024: Microphysical Insights into a Tornadic Supercell from Dual-Polarization Radar Observations in Jiangsu, China on 14 May 2021. *Journal of Meteorological Research*, **38 (2)**, 303–320, https://doi.org/10.1007/s13351-024-3102-5.